Inorganic Chemistry

pubs.acs.org/IC Article

The Chemistry of Acylgermanes: Triacylgermenolates Represent Valuable Building Blocks for the Synthesis of a Variety of Germanium-Based Photoinitiators

Philipp Frühwirt, Andreas Knoechl, Michael Pillinger, Stefanie M. Müller, Perry T. Wasdin, Roland C. Fischer, Judith Radebner, Ana Torvisco, Norbert Moszner, Anne-Marie Kelterer, Thomas Griesser, Georg Gescheidt, and Michael Haas*

Cite This: *Inorg. Chem.* 2020, 59, 15204−15217

Read Online

ACCESS | Metrics & More | Article Recommendations | Supporting Information

ABSTRACT: The formation of a stable triacylgermenolate **2** as a decisive intermediate was achieved by using three pathways. The first two methods involve the reaction of KO*t*Bu or alternatively potassium with tetraacylgermane **1** yielding **2** via one electron transfer. The mechanism involves the formation of radical anions (shown by EPR). This reaction is highly efficient and selective. The third method is a classical salt metathesis reaction toward **2** in nearly quantitative yield. The formation of **2** was confirmed by NMR spectroscopy, UV−vis measurements, and X-ray crystallography. Germenolate **2** serves as a starting point for a wide variety of organo-germanium compounds. We demonstrate the potential of this intermediate by introducing new types of Ge-based photoinitiators **4b**−**4f**. The UV−vis absorption spectra of **4b**−**4f** show considerably increased band intensities due to the presence of eight or more chromophores. Moreover, compounds **4d**−**4f** show absorption tailing up to 525 nm. The performance of these photoinitiators is demonstrated by spectroscopy (time-resolved EPR, laser flash photolysis (LFP), photobleaching (UV−vis)) and photopolymerization experiments (photo-DSC measurements).

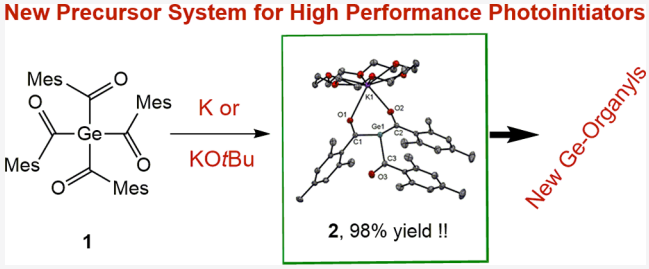

INTRODUCTION

In organic as well as in inorganic chemistry, alkoxides of alkali metals are widely used as powerful bases. Recently, these alkoxides were also found to be involved in a wide variety of reactions where single electron transfer reactions take place.[1−50] In his landmark work, Murphy et al.[51] explained the controversial electron transfer from KO*t*Bu to benzophenone (compare Scheme 1). They showed that KO*t*Bu and benzophenone form a metastable complex, which absorbs light above 400 nm. The light-induced activation results in an electron transfer from the alkoxide to benzophenone, which leads to the formation of a radical anion. Subsequently, the *tert*-butoxy radicals undergo a fragmentation to form acetone and methyl radicals, which were trapped by unreacted benzophenone.[51]

Scheme 1. Photochemical Induced SET of Benzophenone with KO*t*Bu

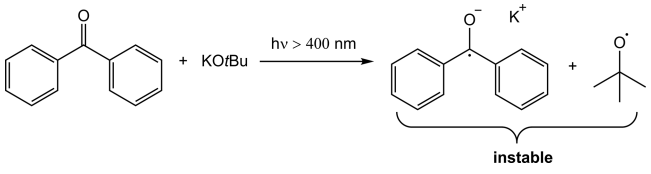

Benzophenone and related derivatives are frequently applied as photoinitiators for UV-curing of inks and coatings.[52] In this context, the keto-derivatives of main group IV organometalloids (mainly germanium-based) have also attracted considerable attention as visible light induced photoinitiators.[53−58] To date, di- and tetraacylgermanes are well established (see Chart 1), although both compound classes have significant drawbacks.

The synthetic pathway for all commercially available diacylgermanes (e.g., Ivocerin) relies on a multistep synthesis (based on the Corey−Seebach reactions), which results in a complex purification process. Tetraacylgermanes, on the other hand, have a low solubility in various monomers, which excludes them from several applications. Therefore, these systems cannot fully meet the requirements for photoinitiators

Received: July 21, 2020
Published: September 29, 2020

https://dx.doi.org/10.1021/acs.inorgchem.0c02181
Inorg. Chem. 2020, 59, 15204−15217

Chart 1. State-of-the-Art Germanium-Based Photoinitiators

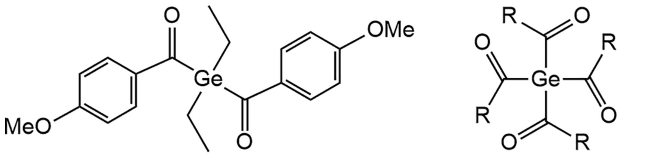

Diacylgermanes (e. g. Ivocerin) Tetraacylgermanes

in high-throughput polymer synthesis. To overcome the above-mentioned restrictions, we further studied reactivities of acylgermanes to develop new pathways toward oligoacylgermanes.

Recently, we investigated the redox chemistry of acylgermanes and discovered their "dark side." Upon reduction with metallic potassium under inert conditions, the corresponding acylgermane radical anions are formed (see Scheme 2), which

Scheme 2. Alkali Metal Reduction of Acylgermanes to the Corresponding Radical Anions

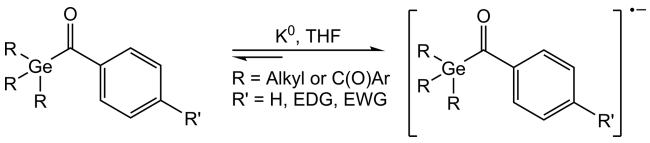

were characterized by EPR spectroscopy in combination with DFT calculations.[59] While monoacylgermanes display similar reduction potentials as benzaldehyde derivatives, the di- and tetraacylgermanes can be reduced at less negative potentials due to the presence of more electron-withdrawing acyl groups.[59]

On the basis of the accessibility of acylgermanium based radical anions and taking into account the seminal work of Murphy and co-workers, merging the chemistry of strong bases and electron transfer, we now explore whether the reduction of acylgermanes provides synthetically attractive reaction pathways.

Our results show a novel aspect of acylgermane chemistry. The aim of this work is to demonstrate that triacylgermenolates can serve as new building blocks for the formation of high performance group-14-based photoinitiators. Additionally, this pathway significantly expands the number of available acylgermanes. Finally, the performance of these photoinitiators was evaluated by spectroscopy (time-resolved EPR), laser flash photolysis (LFP), photobleaching (UV−vis), and photopolymerization experiments (photo-DSC measurements).

RESULTS AND DISCUSSION

Reaction of 1 with K^0 (Method 1). Our first task was to explore the reactivity of **1** with potassium. Therefore, **1** was dissolved in THF, and solid freshly cleaned potassium was added. The surface of the potassium became immediately reddish, which indicates the beginning of the reaction. After approximately 5 min, the yellow reaction solution became orange. The full consumption of the potassium marks the end of the reaction, which results in the formation of hitherto unknown triacylgermenolate **2**. This germenolate was obtained with remarkable selectivity. The obtained THF solution could be stored for prolonged periods (usually days). Analytical and spectroscopic data that strongly support the structural assignment are given in the Experimental Section, together with experimental details.

The reduction potential of **1** (−1.57 V vs SCE in DMF[59]) falls well in line with the reduction potentials observed for other tetraacylgermanes, for which radical anions could be detected by EPR spectroscopy.[59] Therefore, we investigated a THF solution of **1** after exposure to metallic potassium by EPR spectroscopy and could obtain an EPR spectrum (SI, Figure S14). The unresolved EPR signal (g = 2.0039) is likely caused by the formation of tight ion pairs between the ketyl-type radical anions and the magnetically active ^{39}K nuclei (I = 3/2; natural abundance 93.3%) in ethereal solvents (like THF).[60] Generally, the interaction of a ^{39}K nucleus in an ion pair between a radical anion and a K^+ counterion leads to four equidistant lines (1:1:1:1) with a very small hyperfine coupling constant. Accordingly, these lines only rarely appear resolved in the EPR spectra and, in most cases, lead to line broadening. This is in accordance with observations on the related radical anions of TPO ((2,4,6-trimethylbenzoyl)diphenylphosphane oxide) and BAPO (2,4,6-bis(trimethylbenzoyl)-phenylphosphane oxide). Whereas electrochemically (in CH_3CN with Bu_4NClO_4 as supporting electrolyte) generated radical anions where the Bu_4N^+ counterions have no close interaction with the radical anion revealed well-resolved spectra, reduction with K metal in THF leads to severely broadened lines caused by tight ion-pair formation with K^+.[61]

Electron Transfer Reaction Mechanism. On the basis of the above-mentioned observations, Scheme 3 presents a

Scheme 3. SET Reaction of 1 with K^0 (Method 1)

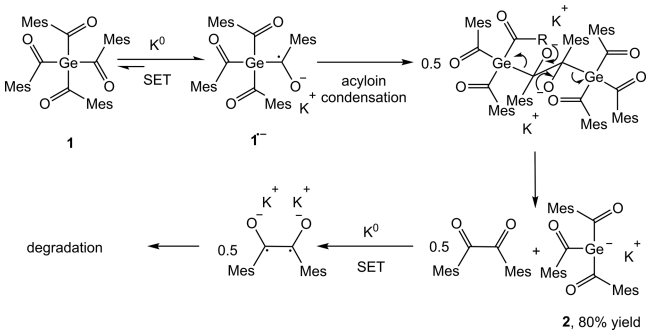

plausible single electron transfer (SET) mechanism for the formation of **2** with the use of potassium as a reduction agent. In the initial reaction step, the radical anion is formed via an SET reaction. This radical anion undergoes an acyloin condensation and after elimination of the diketone, the germenolate **2** is formed. A second SET reaction probably leads to the formation of a diradical, which undergoes a complex and uncharacterized degradation sequence.

In order to prove our mechanism, a trapping experiment with MeI was performed. The reaction solution was quenched with an excess of MeI. The expected triacylgermane **3** was obtained in a very selective fashion alongside uncharacterisable degradation products deriving from the diketone intermediate (Scheme 4).

Reaction of 1 with KO*t*Bu (Method 2). Following the work of Murphy et al., we explored the reactivity of **1** with KO*t*Bu. On the one hand KO*t*Bu is, in comparison to potassium, significantly easier to handle and, on the other hand, a more selective reducing reagent than potassium. Therefore, **1** was dissolved in C_6D_6 in the presence of [18]-

https://dx.doi.org/10.1021/acs.inorgchem.0c02181
Inorg. Chem. 2020, 59, 15204−15217

Scheme 4. Reaction of 2 with MeI

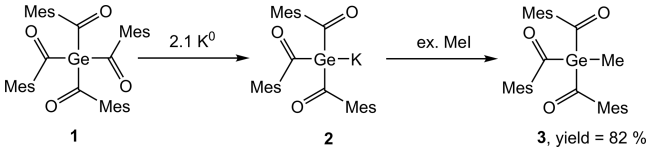

crown-6, and solid KO*t*Bu was added. The reaction solution became immediately reddish, which indicates the beginning of the reaction. After approximately 60 min, the mixture became clear, which indicates the full consumption of the KO*t*Bu. This marks the end of the reaction and again the selective formation of **2** alongside the corresponding ester. Also, this obtained solution could be stored for prolonged periods (usually days). Analytical and spectroscopic data that strongly support the structural assignment are given in the Experimental Section, together with experimental details.

We also obtained a well-resolved EPR spectrum for the mixture of **1**, [18]-crown-6, and KO*t*Bu in C_6D_6 at room temperature (g = 2.0047), which corroborates the formation of *t*BuO$^{\bullet}$ radicals (see SI, Figure S15 and the corresponding discussion below the caption). On the basis of the results from the EPR investigation, we propose a single electron transfer reaction, which allows straightforward access to a radical anion and a *tert*-butoxy radical. Subsequently, these two radicals undergo a hemiketal formation. After elimination of the *tert*-butyl-2,4,6-trimethylbenzoate, the germenolate **2** is formed in excellent yields (see Scheme 5).

Scheme 5. SET Reaction of 1 with KO*t*Bu (Method 2)

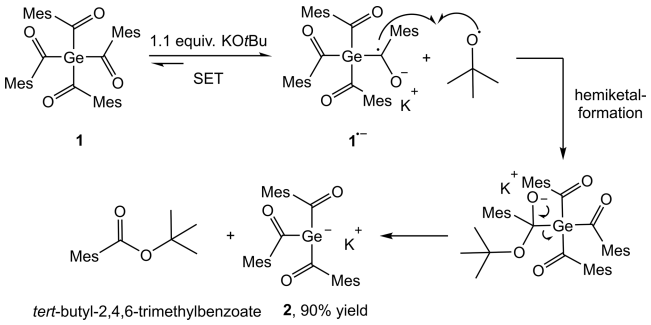

Direct Approach toward 2 (Method 3). As published previously, KO*t*Bu is also of central importance for the formation of tetraacylgermane **1**.[54] During the synthesis of **1**, this strong base cleaves all silicon−germanium bonds in order to form the desired product **1**. On the basis of our new observations that KO*t*Bu also reacts with **1** to form **2**, we reinvestigated the formation of **1**. Indeed, we found that during the synthetic protocol toward **1** (reaction of **4K** with 4 molar equiv of mesitoylfluoride)[54] and prolonged stirring of this mixture (more than 2 days at room temperature), the formation of small amounts of **2** was observed. A complete conversion of **1** to **2** was not detected. Therefore, we set out and reacted the potassium germanide **4K** with 3.0 molar equiv of the mesitoylfluoride, which gave rise to the quantitative formation of **2** within 60 min (see Scheme 6). This direct approach presents a facile synthesis toward **2**. Due to the quantitative formation of **2**, the reaction solution can be directly derivatized with electrophiles.

Scheme 6. Direct Approach toward 2 (Method 3)

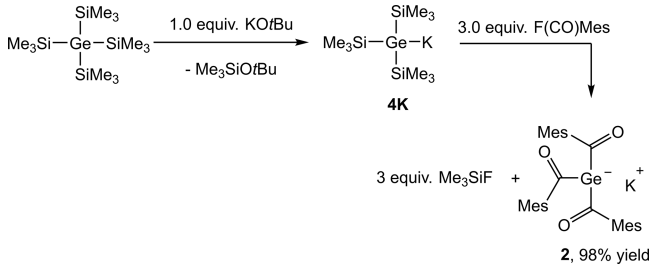

X-ray Crystallography of 2. The structure of **2** was confirmed by single-crystal X-ray diffraction analysis (compare Figure 1 and 2). Figure 1 depicts the standard structure of a

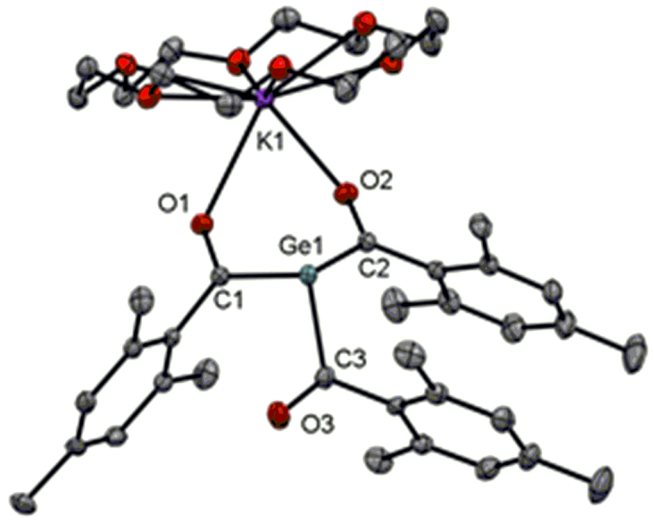

Figure 1. ORTEP representation for compound **2-18-c-6** (1:1 adducts with [18]crown-6). Thermal ellipsoids are depicted at the 50% probability level. Hydrogen atoms are omitted for clarity. Selected bond lengths (Å) and bond angles (deg) with estimated standard deviations: $\sum\alpha$Ge(1) 310.34, Ge(1)−C(1) 2.0137 (12), Ge(1)−C(2) 2.0161 (12), Ge(1)−C(3) 2.0279 (12), C(1)−O(1) 1.2311 (15), C(2)−O(2) 1.2298 (15), C(3)−O(3) 1.2259 (15), K(1)−O(1) 2.7562 (10), K(1)−O(2) 2.7052 (10), K(1)−O(3) 6.289 (10), K(1)−Ge(1) 3.615 (4).

heavier group 14 enolate as a 1:1 adduct of [18]-crown-6. Compound **2-18-c-6** crystallized in the triclinic space group $P\bar{1}$, and the unit cell contains two molecules. Figure 2 shows the first undistorted structure of a heavier group 14 enolate. Compound **2** crystallized in the monoclinic space group $C2/c$, and the unit cell contains eight molecules. As for all other structural characterized germenolates,[62−64] the central Ge atoms of **2-18-c-6** and **2** are pyramidal and have elongated Ge−C single bonds. Particularly striking are two structural features in the structures of **2** with respect to the relative orientation of the three carbonyl groups as well as the distance between the anionic and cationic centers in the molecule. In the case of the **2-18-c-6** derivative, the crown ether is successfully saturating the metal coordination site of the potassium in the equatorial plane, forcing two carbonyl groups to approach the metal center from the axial position. However, in the case of the smaller dimethoxyethane, which is bidentate and considerably less sterically encumbering than the crown ether, the potassium metal is less coordinative saturated and essentially all the carbonyl groups orient themselves in order to

https://dx.doi.org/10.1021/acs.inorgchem.0c02181
Inorg. Chem. 2020, 59, 15204−15217

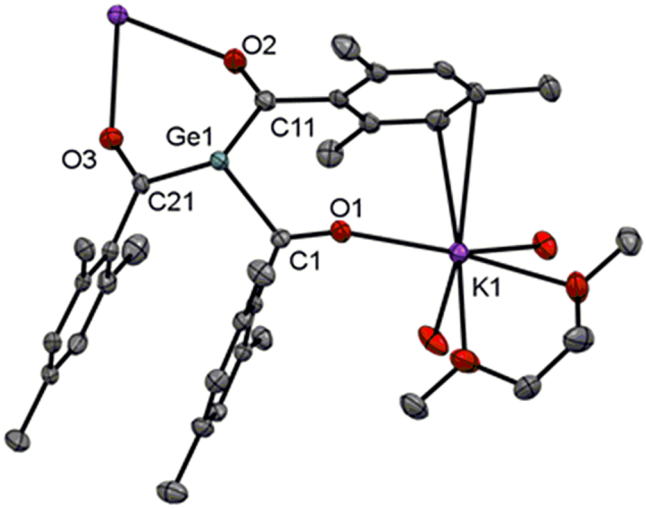

Figure 2. ORTEP representation for compound **2**. Thermal ellipsoids are depicted at the 50% probability level. Hydrogen atoms are omitted for clarity. Selected bond lengths (Å) and bond angles (deg) with estimated standard deviations: ∑αGe(1) 309.13, Ge(1)−C(1) 2.017 (3), Ge(1)−C(11) 2.016 (3), Ge(1)−C(21) 2.011 (3), C(1)−O(1) 1.234 (3), C(11)−O(2) 1.229 (4), C(21)−O(3) 1.232 (3), K(1)−O(1) 2.605 (2), K(1)−O(2) 2.616 (2), K(1)−O(3) 2.648 (2), K(1)−Ge(1) 4.397 (7).

satisfy the coordination sphere of potassium. While the distance between the central germanium atom and the potassium atom in **2-18-c-6** is well in line with all other structural characterized germenolates,[62,63] the distance of the corresponding atoms in **2** is significantly longer (compare Figures 1 and 2). We assume that this is due to the coordination sphere described above.

Stability of 2. Compound **2** can be stored in the absence of air at room temperature for several months without detection of any degradation products. Furthermore, **2** can be completely vacuum-dried. This is in stark contrast to the vacuum instability of all other known heavier group 14 enolates,[64] which undergo degradation reactions during this process. We assume that the remaining acyl groups significantly stabilize the negative charge due to hyperconjugation.

UV−vis Spectroscopy of 2. THF was used as a solvent to determine the charge transfer behavior for the longest wavelength absorption bands.[65] Figure 3 depicts the measured and calculated UV−vis spectra in THF together with their calculated frontier Kohn−Sham orbitals for the HOMO and LUMO orbitals. The germenolate **2** exhibits two intense absorption bands with λ_{max} = 427 nm (band I) and 353 nm (band II). Qualitative agreement between calculated and experimental absorption maxima could be achieved for both bands. In band I, consisting of the first two excitations, the S1 transition is assigned mainly to the HOMO−LUMO excitation. The HOMO mainly corresponds to the p_z orbital of the germanium atom with little variation in shape and energy. Upon excitation, electron density is displaced into the π^* orbital of the carbonyl moieties (LUMO). The next transitions (S2−S5) consist of carbonyl $\pi-\pi^*$ excitations from HOMO−2, HOMO−1, and HOMO into LUMO, LUMO+1, LUMO+2 orbitals with different mixing (see the transition density, the detailed orbital pictures and the interpretation of the spectrum in the Supporting Information).

Reactivity of 2 with Selected Electrophiles. In order to test our new precursor system, we reacted **2** with selected

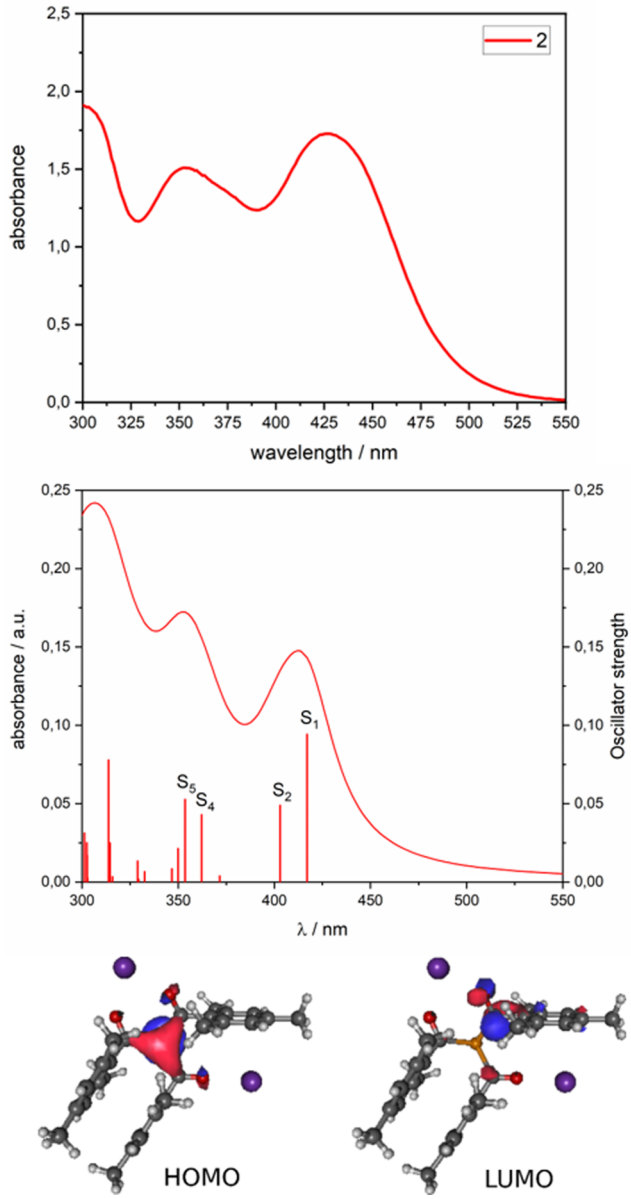

Figure 3. Measured UV−vis spectra of **2** in THF (5×10^{-4} mol/L; top) and calculated absorption spectrum for compound **2** with two K^+'s as counterions. The vertical transitions are marked as vertical lines with their respective oscillator strengths (right axis). The orbitals involved in the first bands are presented.

examples of electrophiles. As suitable electrophiles, we choose aryl- as well as alkyl-substituted di- and triacyl chlorides and two bromo-alkanes. All these reactions resulted in the clean formation of a variety of new oligoacylgermanes in good to excellent yields (compare Scheme 7). These new compounds represent promising high performance photoinitiators. Analytical and spectroscopic data obtained for **4a−4f** are consistent with the proposed structures. NMR spectra and detailed assignments are provided in the Experimental Section and in the Supporting Information. All derivatives show very similar ^{13}C chemical shifts for the carbonyl C atom between δ = 219.5 and 237.6 ppm, which is characteristic for carbonyl groups directly linked to a germanium atom. As method 3 circumvents the usage of [18]-crown-6 and furthermore gives

https://dx.doi.org/10.1021/acs.inorgchem.0c02181
Inorg. Chem. 2020, 59, 15204−15217

Scheme 7. Reaction of 2 with Selected Electrophiles

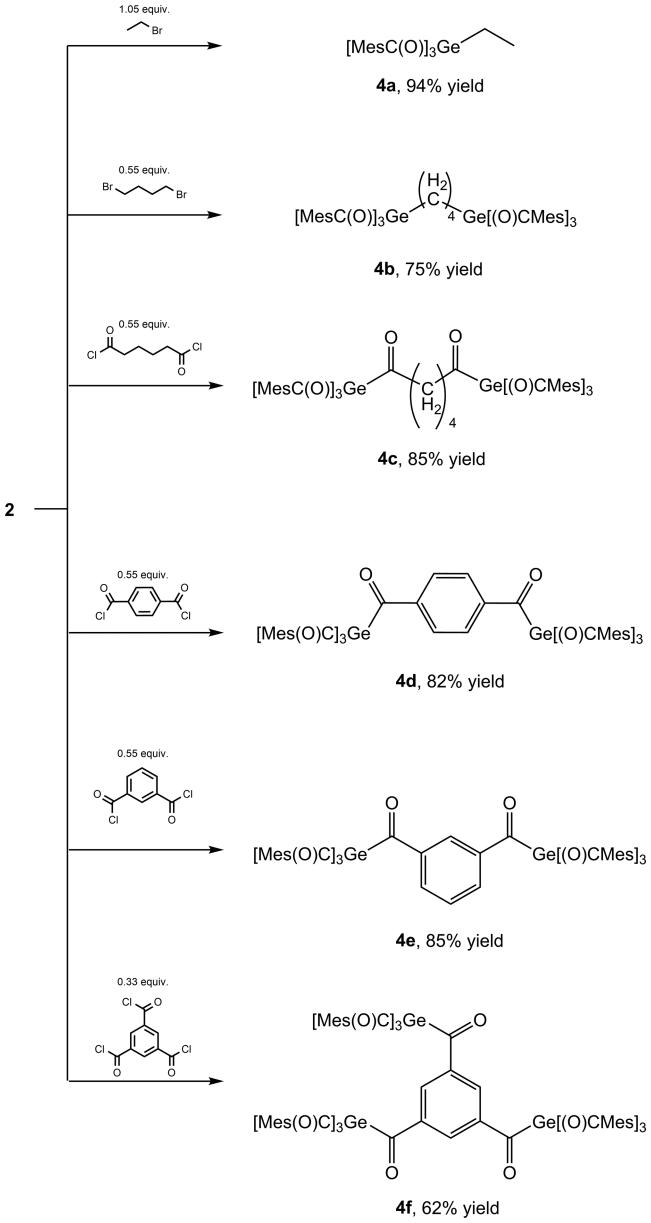

higher yields, this method was used for our reactions with electrophiles.

Crystals suitable for single-crystal X-ray diffraction analysis were obtained for compounds **4b**, **4d**, and **4e**. As a representative example, the molecular structure of **4d** is depicted in Figures 4. All other structures are included in the Supporting Information. Structural data are in accordance with literature values of other acyl germanium compounds.[54,62,63,66] A structural feature, which significantly influences the optical properties, is the torsion angle between the C═O groups and the aromatic ring planes. As a representative example, we discuss the structure of **4d**, which has two substituted carbonyl groups. The six mesityl substituted carbonyl groups have a torsion angle of 57.70°. The two 1,4-phenyl substituted carbonyl groups adopt an angle of 20.94°. The smaller the angle, the more pronounced the conjugation between the aromatic ring and the carbonyl group that is possible, and this results in a bathochromic shift of λ_{max}.

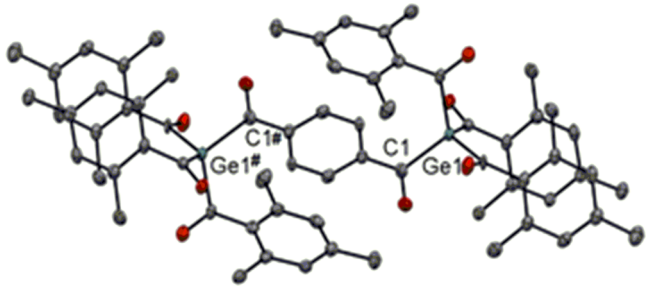

Figure 4. ORTEP representation for compound **4d**. Thermal ellipsoids are depicted at the 50% probability level. Hydrogen atoms are omitted for clarity. Selected bond lengths (Å): d_{Ge-C}(mean) = 2.028, d_{C-O}(mean) = 1.211.

UV/vis Spectroscopy of 4a−4f. To further elucidate substituent effects on the absorption behavior of these new oligoacylgermanes, UV−vis absorption spectra of **4a−4f** were recorded (compare Figure 5). As previously shown for this compound class, the absorption behavior is strongly influenced

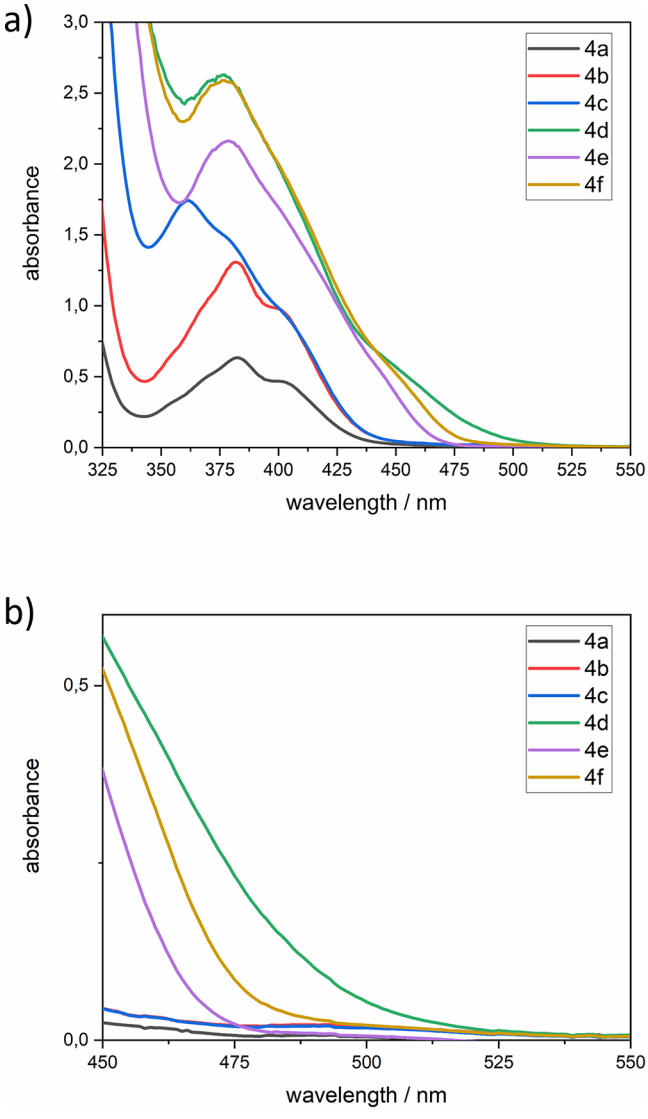

Figure 5. (a) UV/vis absorption spectra of **4a−4f**; dichloromethane solution, $c = 5 \times 10^{-4}$ mol/L, and (b) expanded tails of $n/\sigma-\pi^*$ transition bands.

https://dx.doi.org/10.1021/acs.inorgchem.0c02181
Inorg. Chem. 2020, 59, 15204−15217

by the substitution pattern at the aromatic ring system. In comparison to the tetraacylgermane **1**[54] and the triacylgermane **4a**, all oligoacylgermanes **4b**–**4f** showed a significant higher extinction coefficient, which can be attributed to the higher number of chromophores in the molecule. Moreover, the oligoacylgermanes **4d**–**4f**, where the two triacylgermyl moieties are connected via a dicarbonyl–phenyl bridge, display a substantial red-shift of the absorption edge. The *para*-substitution of compound **4d** induces the bathochromic shifted absorption edge, which shows absorption up to 525 nm (see Table 1). In contrast, the traditional phosphorus-based photoinitiators TPO and BAPO do not absorb above 420 and 440 nm, respectively.[66]

Table 1. Experimental Wavelength Absorption Maxima λ [nm], Extinction Coefficients ε [L·mol^{-1}·cm^{-1}] for 1 and 4a–4f (Dichloromethane)

	$\lambda_{max,exp}$ [nm] (n/σ–π^*(CO/aryl))	ε [L·mol^{-1}·cm^{-1}]
1	375, 408	1485, 938
4a	382, 402	1303, 938
4b	382, 400	2628, 1982
4c	363, 400	3464, 1960
4d	377, 434sh	5252, 1645
4e	379, 394sh	4328, 3642
4f	381, 434sh	5142, 1776

Characterization of Oligoacylgermane Photoinitiators. In the following paragraphs, the photochemical performance of the newly synthesized oligoacylgermanes is investigated. Compound **4a** has been already characterized in a previous publication,[66] and the low solubility of compound **4c** prevents the further characterization of this compound.

Detection of Primary Radicals. Laser-flash photolysis (λ = 355 nm) of the compounds **4b** and **4d**–**4f** (4 mM in toluene) yields TR-EPR (time-resolved electron paramagnetic resonance) spectra, which are compared to the TR-EPR spectrum of tetramesitoylgermane **1**. In all five spectra, the typical unresolved signal from the mesitoyl radical **M**$^{\bullet}$ (g = 2.000) is present (see Figure 6 and Supporting Information). The TR-EPR spectrum of **4b** shows additional peaks, which can be attributed to the germyl radical featuring a CH_2 group adjacent to the Ge center (triplet (1:2:1), a = 0.53 mT, g = 2.003) as shown in Figure 6. This value is in good agreement with the hyperfine coupling constants observed for the related germyl radicals originating from **4a** (triplet, a = 0.44 mT) and bis(*p*-methoxybenzoyl)diethylgermane (BMDG, Ivocerin), which shows a quintet (two CH_2 groups, a = 0.5 mT).[66] Most of the spin density in the germyl radical **Ge(4b)**$^{\bullet}$ is found at the Ge center, as DFT calculations show (see Figure S32 and the corresponding discussion in Supporting Information).

In the case of **1** and **4d**–**4f** with no protons adjacent to the germanium center, relatively narrow and unresolved peaks are expected for the germyl radicals. Accordingly, the intensive EPR signal detected upon photolysis of **1** and **4d**–**4f** represents a superposition of the benzoyl and germyl radical.

Kinetics of the Addition to Double Bonds. Laser-flash photolysis[67] (λ = 355 nm) was used for observing the short-lived germyl radicals and determining the kinetics of their addition to double bonds (of styrene and butyl acrylate) using a pseudo-first-order analysis. At first, the transient optical absorption spectra were acquired for **4b** and **4d**–**4f** (see Supporting Information). The spectra show absorption bands

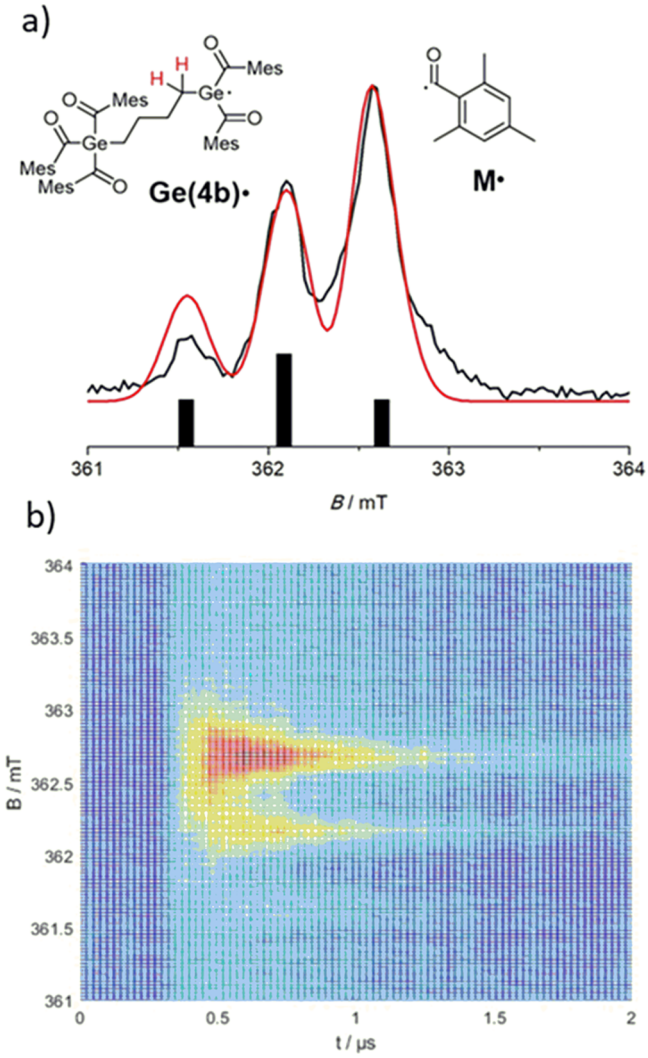

Figure 6. (a) TR-EPR spectrum of **4b** (4 mM in toluene) in the time span of 500 to 1300 ns (black). Red: simulation of the spectrum. The black bars indicate the splitting due to the protons marked in red. (b) Full time profile of the spectrum.

in the area around 350 nm and also between 400 and 500 nm. This latter absorption is characteristic for germyl radicals.[53,66,68] Absorptions of the mesitoyl radical are centered in the UV range and therefore do not interfere with the germyl radicals.[69,70]

Following an exponential fitting to the decay curves of the transient optical absorptions (at the maxima), the pseudo-first-order rate constants k_{exp} were obtained. The second-order addition rate constant $k_{monomer}$ was then determined by using the following relation, where k_0 is the rate constant for the decay in the absence of a monomer:[53,71]

$$k_{exp} = k_0 + k_{monomer} \cdot c_{monomer} \quad (1)$$

The linear fits are displayed in the Supporting Information and the obtained values for $k_{monomer}$ are shown in a bar chart in Figure 7. The numerical values are listed in Table S2 (Supporting Information). For **1**, which serves as a reference, the obtained value in this work (in toluene) is lower than the value in acetonitrile.[66] This is in agreement with observations made by Neshchadin et al.[53] who found that the addition rate

https://dx.doi.org/10.1021/acs.inorgchem.0c02181
Inorg. Chem. 2020, 59, 15204–15217

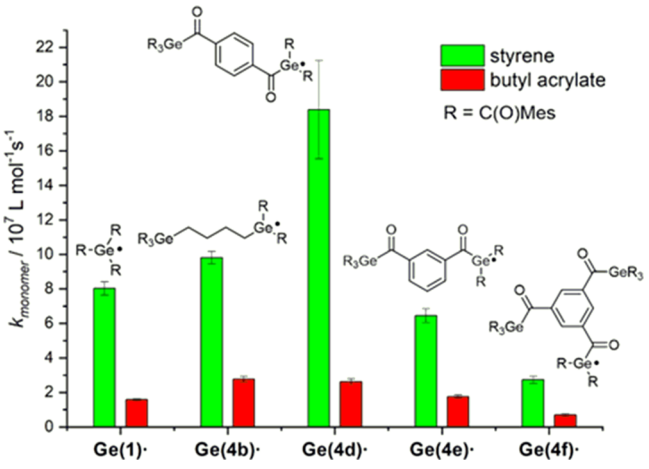

Figure 7. Bar graph of the second-order addition rate constants for the germyl radicals **Ge(1)•**, **Ge(4b)•**, and **Ge(4d–4f)•** to the monomers styrene (green bars) and butyl acrylate (red bars) and their respective structures.

for $Et_2BzGe^•$ to butyl acrylate is slightly higher in acetonitrile than in toluene.

The rate constants for the addition of the germyl radicals to the electron-poor double bond of butyl acrylate decrease in the following order: **Ge(4b)•** ≈ **Ge(4d)•** > **Ge(4e)•** > **Ge(1)•** > **Ge(4f)•**. This is in agreement with observations made in a previous publications by our groups.[66] The more sterically congested the Ge center, the lower is the reactivity toward double bonds (e.g., in Table S2 in the Supporting Information, compare **Ge(1)•** bearing three mesitoyl groups with **Ge(4a)•** featuring two mesitoyl groups and one ethyl group). **Ge(4b)•** comprises an alkyl substituent (or bridge) at the Ge center (comparable to **Ge(4a)•**) resulting in an increased reactivity compared to **Ge(1)•**. Replacing one of the mesitoyl groups with a *para*-dicarbonyl benzene bridge (**Ge(4d)•**) also leads to a higher addition rate constant, since the bridge is sterically less demanding than a mesitoyl group. This effect is only slightly pronounced in **Ge(4e)•**, where the carbonyl groups in the bridge are in a *meta* position to each other. The lowest rate is seen for **Ge(4f)•**, which is the heaviest and bulkiest germyl radical in this row.

Previous investigations[66] indicate that germyl radicals derived from mono- to tetraacylgermanes prefer electron-rich double bonds (e.g., higher rate constants for the addition to methyl methacrylate compared to butyl acrylate). To inspect whether this trend is also evident for the oligoacylgermanes, we choose the electron-rich double bond of styrene as a second reaction partner. Indeed, the addition rate constants increase for all investigated germyl radicals. In the case of **Ge(4d)•**, a multiplication by a factor of 7 is observed, compared to the other germyl radicals, where the factor is between 3.5 and 4. The higher addition rate constant toward styrene suggests that the germyl radicals show electrophilic behavior—a feature which they share with phosphanoyl radicals derived from bis(acyl)phosphane oxide photoinitiators.[72] Accordingly, their addition rate constants toward butyl acrylate are on the same order of magnitude as those of TPO and BAPO (see Table S2 in the Supporting Information).[71]

Photobleaching and Quantum Yields. To avoid colored polymers and reach high curing depths, efficient photobleaching of the photoinitiator is desirable.[66] Solutions of compounds **1**, **4b**, **4d–4f** and the well-characterized bisacylgermane BMDG (Ivocerin) in a mixture of toluene and methyl methacrylate (MMA) were photolyzed with LEDs. The use of MMA and the additional deoxygenation of the samples (with argon) have the purpose of suppressing the formation of undesired (colored) photoproducts, which interfere with the UV–vis measurements.[66]

First, we photolyzed the solutions with an LED emitting at 385 nm (LED385, see Experimental Section for details), since all the studied compounds absorb strongly at this wavelength (see Figure 5). To ensure good comparability, the concentrations of the compounds were adjusted so that A_{385} ≈ 0.7. The results (normalized absorbance as a function of time) are shown in Figure 8a. All compounds show nearly identical time

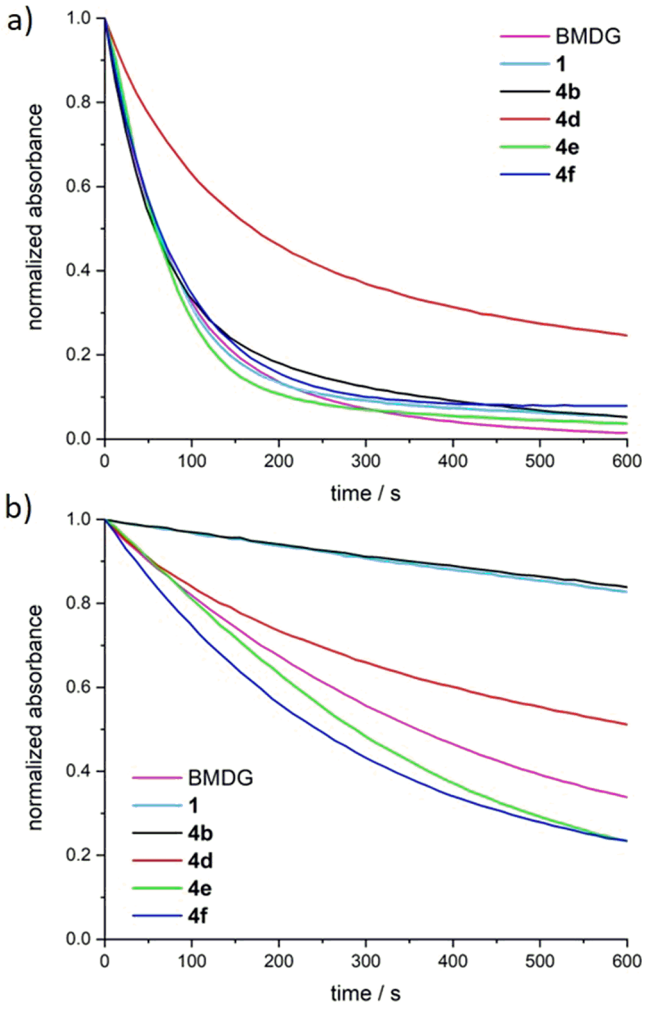

Figure 8. Steady-state photolysis of BMDG and **1**, **4b**, and **4d–4f** with (a) LED385, (b) LED470 in toluene/MMA (1:1 v/v). The absorbance traces are normalized to the initial absorptions at the observation wavelengths (maxima of $n/\sigma-\pi^*$ transitions; BMDG, 412.0 nm; **1**, 378.0 nm; **4b**, 384.0 nm; **4d**, 379.5 nm; **4e**, 380.5 nm; **4f**, 381.0 nm).

traces when irradiating with LED385, except for the *para*-substituted digermane **4d**, whose absorbance decays much slower than the absorbances of the other compounds, so that a slight yellow color is still visible after 600 s.

Since compounds **4d–4f** feature absorbance peaks with considerable tailings up to 500 nm, we also photolyzed solutions of the investigated compounds with an LED emitting

https://dx.doi.org/10.1021/acs.inorgchem.0c02181
Inorg. Chem. 2020, 59, 15204–15217

at 470 nm (LED470; mimicking the longest wavelength emission of dental lamps, see Experimental Section for details).[73] The results are shown in Figure 8b—**4e** and **4f** bleach most efficiently, followed by BMDG and **4d**. Compounds **1** and **4b** do not show substantial absorbance at 470 nm, hence a slow decay is observed. The UV−vis spectra, which were acquired while irradiating the samples with the LEDs, are found in the Supporting Information.

From the data obtained in the photolysis experiments with LED385, the decomposition quantum yields were determined following the procedure by Stadler et al.[74] For each compound, the absorbance trace obtained during irradiation with LED385 was converted to a concentration trace using the extinction coefficients given in Table 2 and then fitted with a monoexponential function ($y = y_0 + A\ e^{k_{fit}x}$) as shown in the Supporting Information. The product of the time constant k_{fit} (in s^{-1}) and the initial concentration of the compound c_0 (in mol L^{-1}) are then divided by the product of the photon flux I_0 (LED385 operated at 45 mA; $I_0 = 1.7 \times 10^{-5}$ mol L^{-1} s^{-1}) and the factor ($1-10^{-A_i'}$), where A_i' is the absorbance at the peak wavelength of the LED (387 nm, see Experimental Section), to obtain the quantum yield:[74]

$$\phi = \frac{k_{fit} c_0}{I_0(1 - 10^{-A_i'})} \quad (2)$$

The calculated quantum yields are shown in Table 2. For BMDG, the obtained quantum yield is almost identical to the value in acetonitrile/MMA.[66] The second highest quantum yield is found for **1**, which is well in line with values found for other tetraacylgermane compounds (ϕ = 0.34−0.44;[66] in acetonitrile/MMA). For the oligoacylgermanes **4b** and **4d**−**4f**, the determined quantum yields range from 0.08 (**4d**) to 0.27 (**4b**). Compared to BMDG, the quantum yields of the oligoacylgermanes are comparably smaller; however, the high extinction coefficients of the $n/\sigma-\pi^*$ transitions compensate for the low quantum yields giving rise to an effective photobleaching.

Table 2. Wavelength of $n/\sigma-\pi^*$ Absorption Maxima and Extinction Coefficients at $\lambda_{max,exp}$ (in Toluene/MMA 1/1 (v/v)), and Determined Quantum Yields for BMDG, 1, 4b, and 4d−4f

	$\lambda_{max,exp}$[nm]	ε [M^{-1} cm^{-1}] at $\lambda_{max,exp}$	Φ (385 nm)
BMDG	412.0	1001	0.86 ± 0.02 (0.83 ± 0.01[a])
1	378.0	1839	0.38 ± 0.01
4b	384.0	2280	0.27 ± 0.01
4d	379.5	3879	0.08 ± 0.01
4e	380.5	3209	0.23 ± 0.01
4f	381.0	5035	0.13 ± 0.01

[a]value in acetonitrile/MMA 1/1 (v/v) from ref.[66]

Photo-DSC measurements. Photo-DSC is a versatile method for the fast and accurate evaluation of the performance of PIs in polymerizable resins. Various characteristic kinetic parameters can be obtained with one single measurement including the time to reach the maximum heat flow (t_{max}), maximum rate of polymerization ($R_{p,max}$), and time to reach 95% of final conversion ($t_{95\%}$). Furthermore, the double bond conversion (DBC) can be calculated from the overall reaction enthalpy ΔH (peak area), providing that the theoretical heat of polymerization ($\Delta H_{0,p}$) is known.

Photo-DSC has been chosen to evaluate the performance of the synthesized photoinitiators in 1,6-hexanediol diacrylate (HDDA) as model monomer system. The previously reported tetraacylgermane **1** was investigated as a reference compound.[54]

The PI performance was compared at equal molar PI concentrations (0.30 mol %) as well as equal amounts of photocleavable groups (0.15 mol % for **1**; 0.2 mol % for **4a**; 0.1 mol % for **4b**; 0.075 mol % for **4d** and **4e**; 0.05 mol % for **4f**; see Figure 9). All investigated PIs show nearly identical behavior for both measurement series. This indicates that the use of lower molar concentrations is possible without negative effects on the observed photoreactivity. Only at very low concentrations, we see a reduction in conversion speed for **1**, **4a**, and **4b** as shown in Table S4. Compound **4d** exhibits a slightly lower DBC in both measurement series, which is consistent with the reduced photobleaching ability and low quantum yield (see Figure 8a and Table 2).

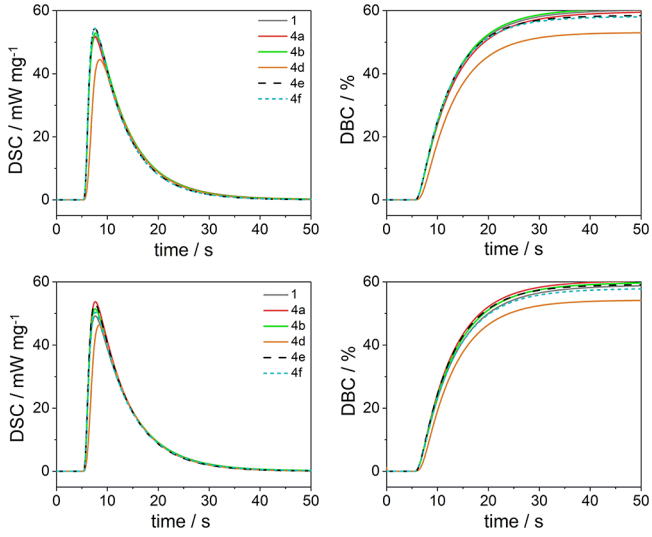

Figure 9. Photo-DSC (left) and conversion plots (right) for the photopolymerization of HDDA with 0.3 mol % PI (top) and PI concentration with equimolar amounts of photocleavable groups (bottom).

CONCLUSION

In summary, we investigated the single electron transfer reactions of tetraacylgermanes induced by potassium or KO*t*Bu. We detected the formation of radicals (by EPR), which act as intermediates for the formation of a stable triacylgermenolate **2**. The one-pot synthetic protocol gives **2** at an excellent yield, as confirmed by NMR spectroscopy, UV−vis measurements, and X-ray crystallography. Furthermore, we could determine the crystal structure of **2**, which represents the first undistorted structure of a heavier group 14 enolate. The efficiency of **2** to serve as new germanium centered precursor system is demonstrated by the reactions with a variety of electrophiles. In all cases, the salt metathesis reaction gave rise to novel acylgermanes in excellent yields. These new acylgermanes were examined for application as high performance photoinitiators. In comparison to **1**, **4b**−**4f** show a significant bathochromic shift of the absorption edge.

https://dx.doi.org/10.1021/acs.inorgchem.0c02181
Inorg. Chem. 2020, 59, 15204−15217

Furthermore, **4b**−**4f** also outperform **1** in terms of extinctions coefficients, resulting in a possible lower consumption of these high priced photoinitiators with the same performance. The data obtained from TR-EPR spectroscopy clearly show that the newly synthesized oligoacylgermanes **4b** and **4d**−**4f** undergo bond cleavage upon irradiation with UV light (λ = 355 nm) forming mesitoyl and germyl radicals. The germyl radicals **Ge(4b)•**, **Ge(4d)•**, and **Ge(4e)•** show higher rate constants for the addition to butyl acrylate when compared to the "lighter relative" **Ge(1)•**. When using styrene with its electron-rich double bond as a reaction partner, the rate constants are increased even more. Especially, **Ge(4d)•** as well as **Ge(4b)•** are more reactive toward styrene than **Ge(1)•**. Photolysis experiments show that all compounds except **4d**, which is characterized by a very small quantum yield of decomposition (ϕ = 0.08), bleach efficiently when irradiated with UV light from an LED (emission maximum 387 nm). Due to the substantial absorption around 500 nm, **4e** and **4f** show considerable photobleaching upon illumination with an LED emitting at about 470 nm. The reaction rates and DBC for **4a**, **4b**, **4e**, and **4f** are comparable to those of **1**. Notably, **4e** and **4f** show consistently high photoreactivity even at very low PI concentrations. On the basis of the photochemical characterization of the compounds, we consider **4e** and **4f** as the most promising candidates for the use as photoinitiators. Further studies to probe the scope of this new synthetic pathway are currently in progress. In addition, we are currently testing these new type I photoinitiators for visible light induced photopolymerization because they have the substantial advantage of bleaching, yielding colorless products.

EXPERIMENTAL SECTION

All experiments were performed under a nitrogen atmosphere using standard Schlenk techniques. Solvents were dried using a column solvent purification system.[75] Me_3SiCl (95%), $GeCl_4$ (>98%), KO*t*Bu (>98%), ClCOMes (99%), ClCO(*o*Tol) (98%), C_6H_4-1-4−$(COCl)_2$ (>99%), C_6H_4-1-3−$(COCl)_2$ (>99%), $Br(CH_2)_4Br$ (99%), MeI (>99%) and [18]-crown-6 (99%), toluene (≥99%), toluene-d_8 (99 atom % D), THF-d_8 (99.5 atom % D), $CDCl_3$ (99.8 atom % D), butyl acrylate (≥99%), styrene (≥99%), and methyl methacrylate (99%) were used without any further purification. Tetrakis(trimethylsilyl)-germane,[76] tetraacylgermane **1** and FCOMes were prepared according to published procedures.[54]

^1H, ^{13}C, and ^{29}Si NMR spectra were recorded on either a Varian INOVA 300 spectrometer in C_6D_6, THF-d_8, or $CDCl_3$ solutions and referenced versus TMS using the internal ^2H-lock signal of the solvent. HRMS spectra were run on a Kratos Profile mass spectrometer. Infrared spectra were obtained on a Bruker Alpha-P Diamond ATR Spectrometer from the solid sample. Melting points were determined using a Stuart SMP50 apparatus and are uncorrected. Elemental analyses were carried out on a Hanau Vario Elementar EL apparatus. UV absorption spectra were recorded on a PerkinElmer Lambda 5 spectrometer.

Reaction of 1 with K^0. A vial was charged with 120 mg (0.181 mmol) of **1** and 14.9 mg (0.381 mmol) of K^0. A total of 1 mL of THF-d_8 was added. The reaction mixture was stirred until the solid K^0 was completely consumed. During this process, the color of the reaction mixture changed from yellow to red. At this time, reaction control by NMR spectroscopy showed the conversion of the starting material to the triacylgermenolate **2**. In order to obtain crystals, 48 mg (0.381 mmol) of [18]-crown-6 was added. Subsequently, the solvent was stripped off under a vacuum. Recrystallization from DME afforded 119 mg (80%) of analytically pure **2** as orange powder.

Compound 2. mp: 165−168 °C. Anal. Calcd for $C_{42}H_{57}GeKO_9$: C, 61.70; H, 7.03%. Found: C, 61.82; H, 7.01%. ^{13}C NMR (C_6D_6, TMS, ppm): 261.30 (C═O); 148.45, 134.94 131.48, 128.38 (Aryl-*C*); 70.30 ($-CH_2-CH_2-O-)_6$; 21.31, 20.45 (Aryl-CH_3). ^1H NMR (C_6D_6, TMS, ppm): 6.61 (s, 6H, Mes-*H*); 3.23 (s, 24H, ($-CH_2-CH_2-O-)_6$); 2.49 (s, 18H, Mes−CH_3); 2.19 (s, 9H, Mes−CH_3). ^{13}C NMR (THF-d_8, TMS, ppm): 263.14 (*C*═O); 148.62, 135.41, 131.77, 128.60 (Aryl-*C*); 21.44, 20.46 (Aryl-CH_3). ^1H NMR (THF-d_8, TMS, ppm): 6.41 (s, 6H, Mes-*H*), 2.16 (s, 9H, Mes−CH_3), 2.05 (s, 18H, Mes−CH_3). UV−vis, λ [nm] (ε [L mol^{-1} cm^{-1}]): 427 (3454), 353 (3030). IR (neat), ν(C═O): 1604, 1590, 1555, 1535.

Reaction of 1 with K^0 and Subsequent Quenching with MeI. A vial was charged with 240 mg (0.363 mmol) of **1a** and 29.8 mg (0.762 mmol) of K^0. A total of 4 mL of THF was added. The reaction mixture was stirred until the solid K^0 was completely consumed. During this process, the color of the reaction mixture changed from yellow to red. At this time, reaction control by NMR spectroscopy showed the conversion of the starting material to the triacylgermenolate **2**. Subsequently, the reaction solution was quenched with an excess of MeI. The reaction solution became immediately yellow. After an aqueous work up with 10 mL of a saturated ammonium chloride solution, the organic layer was separated and dried over Na_2SO_4, and the solvents were stripped off with a rotary evaporator. The reaction mixture was then chromatographed on silica gel using ethyl acetate/*n*-heptane 1:20 as a mobile phase to give 157 mg (82%) of the triacylgermane **3** as yellow oil.

Compound 3. Anal. Calcd for $C_{31}H_{36}GeO_3$: C, 70.35; H, 9.07%. Found: C, 70.42; H, 9.12%. ^{13}C NMR ($CDCl_3$, TMS, ppm): 237.14 (*C*═O); 141.74, 139.74 132.53, 128,85 (Aryl-*C*); 21.25, 19.08 (Aryl-CH_3); −1.57 (Ge-CH_3). ^1H NMR ($CDCl_3$, TMS, ppm): 6.71 (s, 6H, Mes-*H*); 2.25 (s, 9H, Mes−CH_3); 2.06 (s, 18H, Mes−CH_3); 0.66 (s, 3H, Ge−CH_3). UV−vis, λ [nm] (ε [L mol^{-1} cm^{-1}]): 382 (1290), 400 (970). IR (neat) ν(C═O): 1671, 1639, 1602, 1599, 1574.

Reaction of 1 with KO*t*Bu. A vial was charged with 120 mg (0.181 mmol) of **1**, 22.4 mg (0.200 mmol) of KO*t*Bu, and 52.7 mg (0.200 mmol) of [18]-crown-6. Subsequently, 3 mL of C_6D_6 was added. During addition of the C_6D_6, the color of the reaction mixture changed from yellow to red. Stirring of the red solution was continued for approximately 1 h. At this time, reaction control by NMR spectroscopy showed the conversion of the starting material to triacylgermenolate **2** and *tert*-butyl 2,4,6-trimethylbenzoate. In order to obtain crystals for **2**, the solvent was stripped off under a vacuum. Recrystallization from DME afforded 134 mg (90%) of analytically pure **2** as orange powder. After removal of the volatile components on a rotary evaporator, the reaction mixture was chromatographed on a precoated TLC plate SIL G-200 UV_{254} to give 33.2 mg (83%) of *tert*-butyl-2,4,6-trimethylbenzoate as colorless oil.

tert-Butyl-2,4,6-trimethylbenzoate. Anal. Calcd for $C_{14}H_{20}O_2$: C, 76.33; H, 9.15%. Found: C, 76.63; H, 9.33%. ^{13}C NMR ($CDCl_3$, TMS, ppm): 169.49 (*C*═O); 138.67, 134.43 132.66, 128.33 (Aryl-*C*); 81.46 ($-C(CH_3)_3$); 28.31 ($-C(CH_3)_3$); 21.14, 19.54 (Aryl-CH_3). ^1H NMR ($CDCl_3$, TMS, ppm): 6.87 (s, 2H, Mes-*H*); 2.35 (s, 6H, Mes−CH_3); 2.30 (s, 3H, Mes−CH_3); 1.63 (s, 9H, $-C(CH_3)_3$). IR (neat), ν(C═O): 1717, 1612.

Direct Approach to 2. A flask was charged with 500.0 mg (1.37 mmol) of tetrakis(trimethylsilyl)germane and 153.5 mg (1.37 mmol) of KO*t*Bu. A total of 10 mL of DME was added. The reaction mixture was stirred for about 1 h. Subsequently, 227.4 mg (1.37 mmol; 1,0 equiv) of mesitoylfluoride was added to this solution and stirred for another 10 min. This addition was repeated two times with the exact same amount of mesitoylfluoride (in total 454.9 mg, 2.0 equiv). After complete addition, the reaction was stirred for another 30 min. At this time, the orange precipitate was filtered off from the reaction solution, which was identified by NMR spectroscopy as triacylgermenolate **2** (note: **2** contains 0.5 molecules of DME). Yield: 862.9 mg (98%) of analytically pure **2** as orange powder.

Compound 2. mp: 154−156 °C. Anal. Calcd for $C_{32}H_{38}GeKO_4$: C, 64.23; H, 6.40%. Found: C, 64.32; H, 6.32%. ^{13}C NMR (THF-d_8, TMS, ppm): 262.77 (*C*═O); 148.62, 135.17, 131.63, 128.44 (Aryl-*C*); 72.76 [$CH_3-O-(CH_2)-]_2$; 58.95 [$CH_3-O-(CH_2)-]_2$; 21.30, 20.33 (Aryl-CH_3). ^1H NMR (THF-d_8, TMS, ppm): 6.39 (s, 6H, Mes-*H*); 3.43 (s, 2H, [$CH_3-O-(CH_2)-]_2$); 3.27 (s, 3H, [$CH_3-O-(CH_2)-]_2$); 2.15 (s, 9H, Mes−CH_3); 2.03 (s, 18H, Mes−CH_3).

https://dx.doi.org/10.1021/acs.inorgchem.0c02181
Inorg. Chem. 2020, 59, 15204−15217

Synthesis of 4a. Compound **2** was prepared according to method 3 with 3.00 g (8.21 mmol) of $(Me_3Si)_4Ge$, 1.01 g of KO*t*Bu (9.03 mmol; 1.1 equiv), and 4.09 g (24.63 mmol; 3,0 equiv) of mesitoylfluoride. Subsequently, this solution was added to 0.98 g (9.03 mmol, 1.10 equiv) of ethyl bromide dissolved in 60 mL of toluene at −30 °C via a syringe. After complete addition, the reaction was allowed to warm up to room temperature. At this time, reaction control by NMR spectroscopy showed the conversion of the starting material to **4a**. After aqueous workup with 50 mL of saturated NH_4Cl, the organic layer was separated and dried over Na_2SO_4 and filtered and the volatile components removed *in vacuo*. The crude product was recrystallized from acetone, yielding 4.19 g (94%) of analytically pure **4a** as yellow crystals.

Compound 4a. mp: 100−103 °C. Anal. Calcd for $C_{32}H_{38}GeO_3$: C, 70.75; H, 7.05%. Found: C, 70.73; H, 7.07%. ^{13}C NMR ($CDCl_3$, TMS, ppm): 237.58 (*C*═O); 142.22, 139.21, 132.51, 128.80 (Aryl-*C*); 21.24, 19.07 (Aryl-CH_3); 10.42 ($GeCH_2$−CH_3), 8.76 ($GeCH_2$−CH_3). ^1H NMR ($CDCl_3$, TMS, ppm): 6.68 (s, 6H, Mes-*H*); 2.25 (s, 9H, Mes−CH_3); 2.07 (s, 18H, Mes−CH_3); 1.38 (q, 2H, Ge−CH_2−CH_3), 1.00 (t, 3H, Ge−CH_2−CH_3). UV−vis, λ [nm] (ε [L mol^{-1} cm^{-1}]): 382 (1303), 402 (938). IR (neat), ν(C═O): 1650, 1628, 1608.

Synthesis of 4b. Compound **2** was prepared according to method 3 with 3.00 g (8.21 mmol) of $(Me_3Si)_4Ge$, 1.01 g of KO*t*Bu (9.03 mmol; 1.1 equiv), and 4.09 g (24.63 mmol; 3.0 equiv) of mesitoylfluoride. Subsequently, this solution was added to 0.98 g (4.51 mmol, 0.55 equiv) of 1,4-dibromobutane dissolved in 60 mL of toluene at −30 °C via a syringe. After complete addition, the reaction was allowed to warm up to room temperature. At this time, reaction control by NMR spectroscopy showed the conversion of the starting material to **4b**. After aqueous workup with 50 mL of saturated NH_4Cl, the organic layer was separated and dried over Na_2SO_4 and filtered and the volatile components removed *in vacuo*. The crude product was recrystallized from *n*-pentane, yielding 3.34 g (75%) of analytical pure **4b** as yellow crystals.

Compound 4b. mp: 180−181 °C. Anal. Calcd for $C_{64}H_{74}Ge_2O_6$: C, 70.88; H, 6.88%. Found: C, 70.92; H, 6.87%. ^{13}C NMR ($CDCl_3$, TMS, ppm): 237.45 (*C*═O), 142.16, 139.30, 132.49, 128.83, (Aryl-*C*), 27.52, 16.75 (−(−CH_2)$_4$−), 21.26, 19.10 (Aryl-CH_3). ^1H NMR ($CDCl_3$, TMS, ppm): 6.68 (s, 12H, Aryl-*H*), 2.26 (s, 18H, Mes−CH_3), 2.04 (s, 36H, Mes-CH_3), 1.13 (bs, 8H, −(CH_2)$_4$−). UV−vis, λ [nm] (ε [L mol^{-1} cm^{-1}]): 400 (1982), 382 (2628). IR (neat), ν(C═O): 1650, 1632, 1627, 1606.

Synthesis of 4c. Compound **2** was prepared according to method 3 with 3.00 g (8.21 mmol) of $(Me_3Si)_4Ge$, 1.01 g of KO*t*Bu (9.03 mmol; 1.1 equiv) and 4.09 g (24.63 mmol; 3,0 equiv) of mesitoylfluoride. Subsequently, this solution was added to 0.83 g (4.51 mmol, 0.55 equiv) of adipoyl chloride dissolved in 60 mL of toluene at −30 °C via a syringe. After complete addition, the reaction was allowed to warm up to room temperature. At this time, reaction control by NMR spectroscopy showed the conversion of the starting material to **4c**. After an aqueous workup with 50 mL of saturated NH_4Cl, the organic layer was separated and dried over Na_2SO_4 and filtered and the volatile components removed *in vacuo*. The crude product was recrystallized from *n*-pentane, yielding 3.98 g (85%) of analytical pure **4c** as yellow crystals.

Compound 4c. mp: 289−293 °C dec. Anal. Calcd for $C_{66}H_{74}Ge_2O_8$: C, 69.50; H, 6.54%. Found: C, 69.58; H, 6.60%. ^{13}C NMR ($CDCl_3$, TMS, ppm): 232.32, 229.56 (*C*═O), 141.75, 139.90, 132.75, 128.91, (Aryl-*C*), 51.22, 2.80 (−(−CH_2)$_4$−) 21.29, 19.17 (Aryl-CH_3). ^1H NMR ($CDCl_3$, TMS, ppm): 6.67 (s, 12H, Aryl-*H*), 2.24 (s, 18H, Mes−CH_3), 2.09 (s, 36H, Mes-CH_3), 1.03 (bs, 4H, −(CH_2)$_4$−). 0.21 (s, 4H, −(CH_2)$_4$−). UV−vis, λ [nm] (ε [L mol^{-1} cm^{-1}]): 400 (1960), 363 (3464). IR (neat), ν(C═O): 1668, 1654, 1644, 1629, 1606.

Synthesis of 4d. Compound **2** was prepared according to method 3 with 3.00 g (8.21 mmol) of $(Me_3Si)_4Ge$, 1.01 g of KO*t*Bu (9.03 mmol; 1.1 equiv), and 4.09 g (24.63 mmol; 3,0 equiv) of mesitoylfluoride. Subsequently, this solution was added to 0.92 g (4.51 mmol, 0.55 equiv) of terephthaloyl chloride dissolved in 60 mL of toluene at −30 °C via a syringe. After complete addition, the reaction was allowed to warm up to room temperature. At this time, reaction control by NMR spectroscopy showed the conversion of the starting material to **4d**. After aqueous workup with 50 mL of saturated NH_4Cl, the organic layer was separated and dried over Na_2SO_4 and filtered and the volatile components removed *in vacuo*. The crude product was recrystallized from acetone yielding 3.91 g (82%) of analytical pure **4d** as yellow crystals.

Compound 4d. mp: 245−247 °C. Anal. Calcd for $C_{68}H_{70}Ge_2O_8$: C, 70.38; H, 6.08%. Found: C, 70.42; H, 6.15%. ^{13}C NMR ($CDCl_3$, TMS, ppm): 231.61, 222.24 (*C*═O), 141.94, 141.33, 140.12, 133.11, 128.87, 128.61 (Aryl-*C*), 21.23, 19.35 (Aryl-CH_3). ^1H NMR ($CDCl_3$, TMS, ppm): 7.52 (s, 4H, Aryl-*H*), 6.56 (s, 12H, Aryl-*H*), 2.15 (s, 18H, Aryl−CH_3), 2.11 (s, 36H, Aryl−CH_3). UV−vis, λ [nm] (ε [L mol^{-1} cm^{-1}]): 434sh (1645), 377 (5252). IR (neat), ν(C═O): 1658, 1643, 1632, 1619, 1607.

Synthesis of 4e. Compound **2** was prepared according to method 3 with 3.00 g (8.21 mmol) of $(Me_3Si)_4Ge$, 1.01 g of KO*t*Bu (9.03 mmol; 1.1 equiv), and 4.09 g (24.63 mmol; 3,0 equiv) of mesitoylfluoride. Subsequently, this solution was added to 0.92 g (4.51 mmol, 0.55 equiv) of isophthaloyl chloride dissolved in 60 mL of toluene at −30 °C via a syringe. After complete addition, the reaction was allowed to warm up to room temperature. At this time, reaction control by NMR spectroscopy showed the conversion of the starting material to **4e**. After aqueous workup with 50 mL of saturated NH_4Cl, the organic layer was separated and dried over Na_2SO_4 and filtered and the volatile components removed *in vacuo*. The crude product was recrystallized from acetone, yielding 4.05 g (85%) of analytical pure **4e** as yellow crystals.

Compound 4e. mp: 207−208 °C. Anal. Calcd for $C_{68}H_{70}Ge_2O_8$: C, 70.38; H, 6.08%. Found: C, 70.50; H, 6.16%. ^{13}C NMR ($CDCl_3$, TMS, ppm): 231.80, 220.55 (C═O), 141.36, 140.21, 139.96, 134.69, 133.11, 128.85, 125.41 (Aryl-*C*), 21.25, 19.37 (Aryl-CH_3). ^1H NMR ($CDCl_3$, TMS, ppm): 7.90 (t, 1H, Aryl-*H*), 7.79−7.76 (dd, 2H, Aryl-*H*), 7.05 (t, 1H, Aryl-*H*), 6.56 (s, 12H, Aryl-*H*), 2.17 (s, 18H, Aryl−CH_3), 2.12 (s, 36H, Aryl−CH_3). UV−vis, λ [nm] (ε [L mol^{-1} cm^{-1}]): 394sh (3642), 379 (4328). IR (neat), ν(C═O): 1656, 1641, 1606, 1577.

Synthesis of 4f. Compound **2** was prepared according to method 3 with 3.00 g (8.21 mmol) of $(Me_3Si)_4Ge$, 1.01 g of KO*t*Bu (9.03 mmol; 1.1 equiv), and 4.09 g (24.63 mmol; 3,0 equiv) of mesitoylfluoride. Subsequently, this solution was added to 0.72 g (2.71 mmol, 0.33 equiv) of benzene-1,3,5-tricarbonyl trichloride dissolved in 60 mL of toluene at −30 °C via a syringe. After complete addition, the reaction was allowed to warm up to room temperature. At this time, reaction control by NMR spectroscopy showed the conversion of the starting material to **4f**. After an aqueous workup with 50 mL of saturated NH_4Cl, the organic layer was separated and dried over Na_2SO_4 and filtered and the volatile components removed *in vacuo*. The crude product was recrystallized from acetone, yielding 2.86g (62%) of analytical pure **4f** as yellow crystals.

Compound 4f. mp: 189−192 °C. Anal. Calcd for $C_{99}H_{102}Ge_3O_{12}$: C, 69.87; H, 6.04%. Found: C, 69.97; H, 6.16%. ^{13}C NMR ($CDCl_3$, TMS, ppm): 231.05, 219.52 (*C*═O), 141.47, 140.67, 139.78, 133.19, 132.66, 128.94 (Aryl-*C*), 21.26, 19.41 (Aryl-CH_3). ^1H NMR ($CDCl_3$, TMS, ppm): 8.05 (s, 3H, Aryl-*H*), 6.55 (s, 18H, Aryl-*H*), 2.14 (s, 27H, Aryl−CH_3), 2.12 (s, 54H, Aryl−CH_3). UV−vis, λ [nm] (ε [L mol^{-1} cm^{-1}]): 434sh (1776), 381 (5142). IR (neat), ν(C═O): 1654, 1639, 1606.

X-ray Crystallography. All crystals suitable for single crystal X-ray diffractometry were removed from a vial or a Schlenk and immediately covered with a layer of silicone oil. A single crystal was selected, mounted on a glass rod on a copper pin, and placed in the cold N_2 stream provided by an Oxford Cryosystems cryostream. XRD data collection was performed for compounds **2-18-c-6**, **2**, **4b**, **4d**, and **4e**, on a Bruker APEX II diffractometer with the use of an IμS microsource (Incoatec microfocus), a sealed tube of Mo Kα radiation (λ = 0.71073 Å), and a CCD area detector. Data integration was carried out using SAINT.[77] Empirical absorption corrections were applied using SADABS.[78,79] The structures were solved with the use

https://dx.doi.org/10.1021/acs.inorgchem.0c02181
Inorg. Chem. 2020, 59, 15204−15217

of the intrinsic phasing option in SHELXT[80] and refined by the full-matrix least-squares procedures in SHELXL[80−84] as implemented in the program SHELXLE.[85] The space group assignments and structural solutions were evaluated using PLATON.[86−88] The solvent of crystallization for compound **4b** was removed from the refinement by using the "squeeze" option available in the PLATON program suite.[88,89] Disorder was handled by modeling the occupancies of the individual orientations using free variables to refine the respective occupancy of the affected fragments (PART).[90] In some cases, the similarity SAME restraint, the similar-ADP restraint SIMU, and the rigid-bond restraint DELU and RIGU, as well as the constraints EXYZ and EADP, were used in modeling disorder to make the ADP values of the disordered atoms more reasonable. Disordered positions for the germanium atom and one of the mesitoyl moieties in compound **4b** were refined using 55/45 split positions. CCDC 1992490−1992494 contain the supplementary crystallographic data for compounds **2-18-c-6**, **2**, **4b**, **4d**, and **4e**, respectively. These data can be obtained free of charge from The Cambridge Crystallographic Data Centre via www.ccdc.cam.ac.uk/data_request/cif. Table S1 contains crystallographic data and details of measurements and refinement for compounds **2-18-c-6**, **2**, **4b**, **4d**, and **4e**.

TR-EPR. Continuous-wave time-resolved EPR (TR-EPR) experiments were performed on a Bruker ESP 300E X-band spectrometer (unmodulated static magnetic field) equipped with a 125 MHz dual channel digital oscilloscope (Le Croy 9400). As the light source, the frequency tripled light of a Nd:YAG laser was used (InnoLas Spitlight 400, 355 nm, operating at 20 Hz, ∼10 mJ per pulse, 8 ns). The setup is controlled by the fsc2 software developed by Dr. J. T. Törring (Berlin). Spectra were recorded by acquiring the accumulated time responses to the incident laser pulses at each magnetic field value of the chosen field range (field steps: 0.25 G, 50 accumulations). Argon-saturated solutions in toluene were pumped through a flat quartz cell positioned in the cavity of the EPR spectrometer using a flow system (flow rate: 4−5 mL min^{-1}).

LFP. The experiments were performed on a LKS80 Laser Flash Photolysis Spectrometer (Applied Photophysics, UK). Samples were excited with the frequency tripled light from a Spitlight Compact 100 (InnoLas, Germany) solid state Nd:YAG laser at 355 nm (∼10 mJ per pulse, 8 ns). Rate constants for the addition of the germyl radicals to the monomer double bonds were determined in pseudo-first-order experiments. To that end, solutions of the compounds in acetonitrile containing monomer concentrations in the range of 0.01 to 0.1 M and providing absorbance of ∼0.3 at 355 nm were prepared. Before the measurements, the solutions were deoxygenated by bubbling with argon. The decay of the germyl radicals was observed at the absorption maxima in the transient absorption spectra.

Steady-State Photolysis and Determination of Quantum Yields. UV−vis spectra were acquired on a TIDAS UV−vis spectrometer equipped with optical fibers and a 1024-pixel diode-array detector (J&M Analytik AG, Essingen, Germany). For the photobleaching experiments, two different LEDs (Roithner Lasertechnik GmbH, Vienna, Austria)—LED385 (emission maximum 387 nm; 15 nm full width at half-maximum; 7.8 mW at 20 mA) and LED470 (emission maximum at 463 nm; 30 nm full width at half-maximum; 7.4 mW at 20 mA)—were used. The output power of the LEDs was determined by a spectrophotometer (GL Spectis, GL Optics, Germany) equipped with an integrating sphere (Ulbricht sphere). Both LEDs were operated at a photon flux of 0.05 μmol s^{-1} to ensure comparability of the results. Solutions of the investigated compounds in a 1:1 (v/v) mixture of toluene and methyl methacrylate (MMA) were filled into 1 cm × 1 cm quartz cuvettes intended for fluorescence measurements and degassed by bubbling with argon for 5 min. Samples were irradiated perpendicular to the optical path of the spectrometer and stirred during the measurements with a magnetic stirring bar (750 rpm). The concentrations of the compounds were between 0.14 and 1.00 mM (within the linear range of the spectrometer). The data acquired in the photobleaching experiment with LED385 were used to determine the quantum yields of decomposition. To that end, the absorbance traces were converted to concentration traces and fitted with a monoexponential function. The setup is described in more detail in ref 74.

Computational Methods. All computational studies were executed with the program ORCA4.0.1.[91] Density functional theory (DFT) was applied using the B3LYP functional[92,93] with inclusion of the dispersion interaction including Becke-Johnson damping (D3BJ).[94,95] The def2-SVP basis set was used for optimization of the geometries, and their harmonic frequencies were calculated to confirm the geometries as minima at the potential energy surface.[96] The basis set def2-TZVPP was used for the computation of the vertical excitations by applying time-dependent density functional theory[97] (TD-DFT) calculations with 20 states. All calculations were performed in the solvent THF in the continuum solvation model CPCM.[98] The geometry of **2** was optimized with one and two potassium counterions by starting from the X-ray conformation. For the UV data, the electronic distribution with two K^+ agreed best with the experimental data. The UV spectra were simulated with a half width at half height of 18 nm, and the molecular orbitals were generated with contour values of 0.05 au, both with the program Gabedit.[99] The hyperfine coupling constants were computed applying the def2-TZVPP basis set with FinalGrid = 7, and the spin density map was drawn with Gabedit.[97]

Photo-DSC Measurements. The photo-DSC measurements were conducted using a Netzsch DSC 204 F1 with an autosampler. The respective amounts of photoinitiator (0.3 and 0.15 mol % for **1**; 0.3 and 0.2 mol % for **4a**; 0.3 and 0.1 mol % for **4b**; 0.3 and 0.075 mol % for **4d** and **4e**; 0.3 and 0.05 mol % for **4f**) were added to the monomer HDDA and mixed in an ultrasonic bath for 30 min at room temperature. A total of 10 ± 1 mg of each formulation was weighed into an open aluminum pan, and all formulations were analyzed in triplicate. The prepared formulations were measured at 25 °C under an inert atmosphere (N_2 flow = 20 mL min^{-1}). After an equilibration phase of 4 min, the samples were irradiated for 6 min with UV light from a Lumen Dynamics OmniCure Series 2001-XLA. The light intensity was set to 1 W cm^{-1}, and the heat flow of the polymerization reaction was recorded as a function of time. From the theoretical heat of polymerization of the monomer HDDA ($\Delta H_{0,HDDA}$ = 761.92 J g^{-1} or 172.4 kJ mol^{-1}, determined from 86.2 kJ mol^{-1} per acrylate unit),[54] the double bond conversion (DBC) was calculated by dividing the measured heat of polymerization ΔH by $\Delta H_{0,HDDA}$. The maximum rate of polymerization $R_{p,max}$ was calculated using eq 3, with h as the height of the exothermic polymerization signal in mW mg^{-1} and ρ = 1010 g L^{-1} as the density of HDDA at 25 °C.

$$R_{p,max} = \frac{h \cdot \rho}{\Delta H_{0,HDDA}} \quad (3)$$

■ ASSOCIATED CONTENT

Supporting Information

The Supporting Information is available free of charge at https://pubs.acs.org/doi/10.1021/acs.inorgchem.0c02181.

NMR spectra, X-ray data, additional graphs, kinetic data, and DFT calculations (PDF)

Cartesian coordinates of calculated structures (XYZ)

Accession Codes

CCDC 1992490−1992494 contain the supplementary crystallographic data for this paper. These data can be obtained free of charge via www.ccdc.cam.ac.uk/data_request/cif, or by emailing data_request@ccdc.cam.ac.uk, or by contacting The Cambridge Crystallographic Data Centre, 12 Union Road, Cambridge CB2 1EZ, UK; fax: +44 1223 336033.

https://dx.doi.org/10.1021/acs.inorgchem.0c02181
Inorg. Chem. 2020, 59, 15204−15217

AUTHOR INFORMATION

Corresponding Author

Michael Haas − *Institute of Inorganic Chemistry, Graz University of Technology, A-8010 Graz, Austria;* orcid.org/0000-0002-9213-940X; Email: michael.haas@tugraz.at

Authors

Philipp Frühwirt − *Institute of Physical and Theoretical Chemistry, Graz University of Technology, A-8010 Graz, Austria*

Andreas Knoechl − *Institute of Inorganic Chemistry, Graz University of Technology, A-8010 Graz, Austria*

Michael Pillinger − *Institute of Inorganic Chemistry, Graz University of Technology, A-8010 Graz, Austria*

Stefanie M. Müller − *Institute of Chemistry of Polymeric Materials, Montanuniversitaet Leoben, A-8700 Leoben, Austria*

Perry T. Wasdin − *Institute of Physical and Theoretical Chemistry, Graz University of Technology, A-8010 Graz, Austria*

Roland C. Fischer − *Institute of Inorganic Chemistry, Graz University of Technology, A-8010 Graz, Austria;* orcid.org/0000-0001-9523-5010

Judith Radebner − *Institute of Inorganic Chemistry, Graz University of Technology, A-8010 Graz, Austria*

Ana Torvisco − *Institute of Inorganic Chemistry, Graz University of Technology, A-8010 Graz, Austria;* orcid.org/0000-0002-6203-7330

Norbert Moszner − *Ivoclar Vivadent AG, FL-9494 Schaan, Liechtenstein*

Anne-Marie Kelterer − *Institute of Physical and Theoretical Chemistry, Graz University of Technology, A-8010 Graz, Austria;* orcid.org/0000-0001-8178-2670

Thomas Griesser − *Institute of Chemistry of Polymeric Materials, Montanuniversitaet Leoben, A-8700 Leoben, Austria;* orcid.org/0000-0002-9493-3770

Georg Gescheidt − *Institute of Physical and Theoretical Chemistry, Graz University of Technology, A-8010 Graz, Austria;* orcid.org/0000-0002-6827-4337

Complete contact information is available at: https://pubs.acs.org/10.1021/acs.inorgchem.0c02181

Notes

The authors declare no competing financial interest.

ACKNOWLEDGMENTS

We gratefully acknowledge financial support from Ivoclar Vivadent AG, NAWI Graz, and FWF (Vienna, Austria; project number P 32606-N).

REFERENCES

(1) Yanagisawa, S.; Ueda, K.; Taniguchi, T.; Itami, K. Potassium t-butoxide alone can promote the biaryl coupling of electron-deficient nitrogen heterocycles and haloarenes. *Org. Lett.* **2008**, *10*, 4673−4676.

(2) Sun, C.-L.; Li, H.; Yu, D.-G.; Yu, M.; Zhou, X.; Lu, X.-Y.; Huang, K.; Zheng, S.-F.; Li, B.-J.; Shi, Z.-J. An efficient organocatalytic method for constructing biaryls through aromatic C-H activation. *Nat. Chem.* **2010**, *2*, 1044−1049.

(3) Shirakawa, E.; Itoh, K.-I.; Higashino, T.; Hayashi, T. tert-Butoxide-mediated arylation of benzene with aryl halides in the presence of a catalytic 1,10-phenanthroline derivative. *J. Am. Chem. Soc.* **2010**, *132*, 15537−15539.

(4) Liu, W.; Cao, H.; Zhang, H.; Zhang, H.; Chung, K. H.; He, C.; Wang, H.; Kwong, F. Y.; Lei, A. Organocatalysis in cross-coupling: DMEDA-catalyzed direct C-H arylation of unactivated benzene. *J. Am. Chem. Soc.* **2010**, *132*, 16737−16740.

(5) Sun, C.-L.; Gu, Y.-F.; Wang, B.; Shi, Z.-J. Direct arylation of alkenes with aryl iodides/bromides through an organocatalytic radical process. *Chem. - Eur. J.* **2011**, *17*, 10844−10847.

(6) Sun, C.-L.; Gu, Y.-F.; Huang, W.-P.; Shi, Z.-J. Neocuproine-KOtBu promoted intramolecular cross coupling to approach fused rings. *Chem. Commun.* **2011**, *47*, 9813−9815.

(7) Shirakawa, E.; Zhang, X.; Hayashi, T. Mizoroki-heck-type reaction mediated by potassium tert-butoxide. *Angew. Chem., Int. Ed.* **2011**, *50*, 4671−4674.

(8) Rueping, M.; Leiendecker, M.; Das, A.; Poisson, T.; Bui, L. Potassium tert-butoxide mediated Heck-type cyclization/isomerization-benzofurans from organocatalytic radical cross-coupling reactions. *Chem. Commun.* **2011**, *47*, 10629−10631.

(9) Qiu, Y.; Liu, Y.; Yang, K.; Hong, W.; Li, Z.; Wang, Z.; Yao, Z.; Jiang, S. New ligands that promote cross-coupling reactions between aryl halides and unactivated arenes. *Org. Lett.* **2011**, *13*, 3556−3559.

(10) Roman, D. S.; Takahashi, Y.; Charette, A. B. Potassium tert-butoxide promoted intramolecular arylation via a radical pathway. *Org. Lett.* **2011**, *13*, 3242−3245.

(11) Shirakawa, E.; Hayashi, T. Transition-metal-free Coupling Reactions of Aryl Halides. *Chem. Lett.* **2012**, *41*, 130−134.

(12) Liu, H.; Yin, B.; Gao, Z.; Li, Y.; Jiang, H. Transition-metal-free highly chemo- and regioselective arylation of unactivated arenes with aryl halides over recyclable heterogeneous catalysts. *Chem. Commun.* **2012**, *48*, 2033−2035.

(13) Chen, W.-C.; Hsu, Y.-C.; Shih, W.-C.; Lee, C.-Y.; Chuang, W.-H.; Tsai, Y.-F.; Chen, P. P.-Y.; Ong, T.-G. Metal-free arylation of benzene and pyridine promoted by amino-linked nitrogen heterocyclic carbenes. *Chem. Commun.* **2012**, *48*, 6702−6704.

(14) De, S.; Ghosh, S.; Bhunia, S.; Sheikh, J. A.; Bisai, A. Intramolecular direct dehydrohalide coupling promoted by KO(t)Bu: total synthesis of Amaryllidaceae alkaloids anhydrolycorinone and oxoassoanine. *Org. Lett.* **2012**, *14*, 4466−4469.

(15) Tanimoro, K.; Ueno, M.; Takeda, K.; Kirihata, M.; Tanimori, S. Proline catalyzes direct C-H arylations of unactivated arenes. *J. Org. Chem.* **2012**, *77*, 7844−7849.

(16) Wu, Y.; Wong, S. M.; Mao, F.; Chan, T. L.; Kwong, F. Y. Intramolecular direct C-H bond arylation from aryl chlorides: a transition-metal-free approach for facile access of phenanthridines. *Org. Lett.* **2012**, *14*, 5306−5309.

(17) Zhao, H.; Shen, J.; Guo, J.; Ye, R.; Zeng, H. A macrocyclic aromatic pyridone pentamer as a highly efficient organocatalyst for the direct arylations of unactivated arenes. *Chem. Commun.* **2013**, *49*, 2323−2325.

(18) Budén, M. E.; Guastavino, J. F.; Rossi, R. A. Room-temperature photoinduced direct C-H-arylation via base-promoted homolytic aromatic substitution. *Org. Lett.* **2013**, *15*, 1174−1177.

(19) Liu, W.; Tian, F.; Wang, X.; Yu, H.; Bi, Y. Simple alcohols promoted direct C-H arylation of unactivated arenes with aryl halides. *Chem. Commun.* **2013**, *49*, 2983−2985.

(20) Kumar, A.; Bhakuni, B. S.; Prasad, C. D.; Kumar, S.; Kumar, S. Potassium tert-butoxide-mediated synthesis of unsymmetrical diaryl ethers, sulfides and selenides from aryl bromides. *Tetrahedron* **2013**, *69*, 5383−5392.

(21) De, S.; Mishra, S.; Kakde, B. N.; Dey, D.; Bisai, A. Expeditious approach to pyrrolophenanthridones, phenanthridines, and benzocphenanthridines via organocatalytic direct biaryl-coupling promoted by potassium tert-butoxide. *J. Org. Chem.* **2013**, *78*, 7823−7844.

(22) Sharma, S.; Kumar, M.; Kumar, V.; Kumar, N. Vasicine catalyzed direct C−H arylation of unactivated arenes: organocatalytic application of an abundant alkaloid. *Tetrahedron Lett.* **2013**, *54*, 4868−4871.

(23) Dewanji, A.; Murarka, S.; Curran, D. P.; Studer, A. Phenyl hydrazine as initiator for direct arene C-H arylation via base promoted homolytic aromatic substitution. *Org. Lett.* **2013**, *15*, 6102−6105.

(24) Wu, Y.; Choy, P. Y.; Kwong, F. Y. Direct intermolecular C-H arylation of unactivated arenes with aryl bromides catalysed by 2-pyridyl carbinol. *Org. Biomol. Chem.* **2014**, *12*, 6820−6823.
(25) Zhou, S.; Doni, E.; Anderson, G. M.; Kane, R. G.; MacDougall, S. W.; Ironmonger, V. M.; Tuttle, T.; Murphy, J. A. Identifying the roles of amino acids, alcohols and 1,2-diamines as mediators in coupling of haloarenes to arenes. *J. Am. Chem. Soc.* **2014**, *136*, 17818−17826.
(26) Guastavino, J. F.; Budén, M. E.; Rossi, R. A. Room-temperature and transition-metal-free Mizoroki-Heck-type reaction. Synthesis of E-stilbenes by photoinduced C-H functionalization. *J. Org. Chem.* **2014**, *79*, 9104−9111.
(27) Bhakuni, B. S.; Yadav, A.; Kumar, S.; Patel, S.; Sharma, S.; Kumar, S. KO(t)Bu-mediated synthesis of dimethylisoindolin-1-ones and dimethyl-5-phenylisoindolin-1-ones: selective C-C coupling of an unreactive tertiary sp3 C-H bond. *J. Org. Chem.* **2014**, *79*, 2944−2954.
(28) Cuthbertson, J.; Gray, V. J.; Wilden, J. D. Observations on transition metal free biaryl coupling: potassium tert-butoxide alone promotes the reaction without diamine or phenanthroline catalysts. *Chem. Commun.* **2014**, *50*, 2575−2578.
(29) Zhou, S.; Anderson, G. M.; Mondal, B.; Doni, E.; Ironmonger, V.; Kranz, M.; Tuttle, T.; Murphy, J. A. Organic super-electron-donors: initiators in transition metal-free haloarene−arene coupling. *Chem. Sci.* **2014**, *5*, 476−482.
(30) Ghosh, D.; Lee, J.-Y.; Liu, C.-Y.; Chiang, Y.-H.; Lee, H. M. Direct C-H Arylations of Unactivated Arenes Catalyzed by Amido-Functionalized Imidazolium Salts. *Adv. Synth. Catal.* **2014**, *356*, 406−410.
(31) Bhakuni, B. S.; Yadav, A.; Kumar, S.; Kumar, S. AMVN-initiated expedient synthesis of biaryls by the coupling reaction of unactivated arenes and heteroarenes with aryl iodides. *New J. Chem.* **2014**, *38*, 827.
(32) Doni, E.; Zhou, S.; Murphy, J. A. Electron transfer-induced coupling of haloarenes to styrenes and 1,1-diphenylethenes triggered by diketopiperazines and Potassium tert-butoxide. *Molecules* **2015**, *20*, 1755−1774.
(33) Masters, K.-S. Multi-bond forming and iodo-selective base-promoted homolytic aromatic substitution. *RSC Adv.* **2015**, *5*, 29975−29986.
(34) Yi, H.; Jutand, A.; Lei, A. Evidence for the interaction between (t)BuOK and 1,10-phenanthroline to form the 1,10-phenanthroline radical anion: a key step for the activation of aryl bromides by electron transfer. *Chem. Commun.* **2015**, *51*, 545−548.
(35) Toutov, A. A.; Liu, W.-B.; Betz, K. N.; Fedorov, A.; Stoltz, B. M.; Grubbs, R. H. Silylation of C-H bonds in aromatic heterocycles by an Earth-abundant metal catalyst. *Nature* **2015**, *518*, 80−84.
(36) Pichette Drapeau, M.; Fabre, I.; Grimaud, L.; Ciofini, I.; Ollevier, T.; Taillefer, M. Transition-Metal-Free α-Arylation of Enolizable Aryl Ketones and Mechanistic Evidence for a Radical Process. *Angew. Chem., Int. Ed.* **2015**, *54*, 10587−10591.
(37) Patil, M. Mechanistic Insights into the Initiation Step of the Base Promoted Direct C-H Arylation of Benzene in the Presence of Additive. *J. Org. Chem.* **2016**, *81*, 632−639.
(38) Ragno, D.; Zaghi, A.; Di Carmine, G.; Giovannini, P. P.; Bortolini, O.; Fogagnolo, M.; Molinari, A.; Venturini, A.; Massi, A. Cross-benzoin and Stetter-type reactions mediated by KOtBu-DMF via an electron-transfer process. *Org. Biomol. Chem.* **2016**, *14*, 9823−9835.
(39) Barham, J. P.; Coulthard, G.; Kane, R. G.; Delgado, N.; John, M. P.; Murphy, J. A. Double Deprotonation of Pyridinols Generates Potent Organic Electron-Donor Initiators for Haloarene-Arene Coupling. *Angew. Chem., Int. Ed.* **2016**, *55*, 4492−4496.
(40) Barham, J. P.; Coulthard, G.; Emery, K. J.; Doni, E.; Cumine, F.; Nocera, G.; John, M. P.; Berlouis, L. E. A.; McGuire, T.; Tuttle, T.; Murphy, J. A. KOtBu: A Privileged Reagent for Electron Transfer Reactions? *J. Am. Chem. Soc.* **2016**, *138*, 7402−7410.
(41) Liu, W.; Hou, F. Transition-metal-free dehalogenation of aryl halides promoted by phenanthroline/potassium tert -butoxide. *Tetrahedron* **2017**, *73*, 931−937.
(42) Budén, M. E.; Bardagí, J. I.; Puiatti, M.; Rossi, R. A. Initiation in Photoredox C-H Functionalization Reactions. Is Dimsyl Anion a Key Ingredient? *J. Org. Chem.* **2017**, *82*, 8325−8333.
(43) Cumine, F.; Zhou, S.; Tuttle, T.; Murphy, J. A. A study of diketopiperazines as electron-donor initiators in transition metal-free haloarene-arene coupling. *Org. Biomol. Chem.* **2017**, *15*, 3324−3336.
(44) Emery, K. J.; Tuttle, T.; Murphy, J. A. Evidence of single electron transfer from the enolate anion of an N, N'-dialkyldiketo-piperazine additive in BHAS coupling reactions. *Org. Biomol. Chem.* **2017**, *15*, 8810−8819.
(45) Banerjee, S.; Yang, Y.-F.; Jenkins, I. D.; Liang, Y.; Toutov, A. A.; Liu, W.-B.; Schuman, D. P.; Grubbs, R. H.; Stoltz, B. M.; Krenske, E. H.; Houk, K. N.; Zare, R. N. Ionic and Neutral Mechanisms for C-H Bond Silylation of Aromatic Heterocycles Catalyzed by Potassium tert-Butoxide. *J. Am. Chem. Soc.* **2017**, *139*, 6880−6887.
(46) Liu, W.-B.; Schuman, D. P.; Yang, Y.-F.; Toutov, A. A.; Liang, Y.; Klare, H. F. T.; Nesnas, N.; Oestreich, M.; Blackmond, D. G.; Virgil, S. C.; Banerjee, S.; Zare, R. N.; Grubbs, R. H.; Houk, K. N.; Stoltz, B. M. Potassium tert-Butoxide-Catalyzed Dehydrogenative C-H Silylation of Heteroaromatics: A Combined Experimental and Computational Mechanistic Study. *J. Am. Chem. Soc.* **2017**, *139*, 6867−6879.
(47) Evoniuk, C. J.; Gomes, G. D. P.; Hill, S. P.; Fujita, S.; Hanson, K.; Alabugin, I. V. Coupling N-H Deprotonation, C-H Activation, and Oxidation: Metal-Free C(sp3)−H Aminations with Unprotected Anilines. *J. Am. Chem. Soc.* **2017**, *139*, 16210−16221.
(48) Lin, S.; He, X.; Meng, J.; Gu, H.; Zhang, P.; Wu, J. An Expedient Synthesis of Carbazoles through Potassium tert -Butoxide-Promoted Intramolecular Direct C-H Bond Arylation. *Eur. J. Org. Chem.* **2017**, *2017*, 443−447.
(49) Smith, A. J.; Young, A.; Rohrbach, S.; O'Connor, E. F.; Allison, M.; Wang, H.-S.; Poole, D. L.; Tuttle, T.; Murphy, J. A. Electron-Transfer and Hydride-Transfer Pathways in the Stoltz-Grubbs Reducing System (KOtBu/Et3 SiH). *Angew. Chem., Int. Ed.* **2017**, *56*, 13747−13751.
(50) Yang, H.; Zhang, L.; Jiao, L. N-Methylanilines as Simple and Efficient Promoters for Radical-Type Cross-Coupling Reactions of Aryl Iodides. *Chem. - Eur. J.* **2017**, *23*, 65−69.
(51) Nocera, G.; Young, A.; Palumbo, F.; Emery, K. J.; Coulthard, G.; McGuire, T.; Tuttle, T.; Murphy, J. A. Electron Transfer Reactions: KO tBu (but not NaO tBu) Photoreduces Benzophenone under Activation by Visible Light. *J. Am. Chem. Soc.* **2018**, *140*, 9751−9757.
(52) Carroll, G. T.; Turro, N. J.; Koberstein, J. T. Patterning dewetting in thin polymer films by spatially directed photo-crosslinking. *J. Colloid Interface Sci.* **2010**, *351*, 556−560.
(53) Neshchadin, D.; Rosspeintner, A.; Griesser, M.; Lang, B.; Mosquera-Vazquez, S.; Vauthey, E.; Gorelik, V.; Liska, R.; Hametner, C.; Ganster, B.; Saf, R.; Moszner, N.; Gescheidt, G. Acylgermanes: photoinitiators and sources for Ge-centered radicals. insights into their reactivity. *J. Am. Chem. Soc.* **2013**, *135*, 17314−17321.
(54) Radebner, J.; Eibel, A.; Leypold, M.; Gorsche, C.; Schuh, L.; Fischer, R.; Torvisco, A.; Neshchadin, D.; Geier, R.; Moszner, N.; Liska, R.; Gescheidt, G.; Haas, M.; Stueger, H. Tetraacylgermanes: Highly Efficient Photoinitiators for Visible-Light-Induced Free-Radical Polymerization. *Angew. Chem., Int. Ed.* **2017**, *56*, 3103−3107.
(55) Ganster, B.; Fischer, U. K.; Moszner, N.; Liska, R. New Photocleavable Structures. Diacylgermane-Based Photoinitiators for Visible Light Curing. *Macromolecules* **2008**, *41*, 2394−2400.
(56) Ganster, B.; Fischer, U. K.; Moszner, N.; Liska, R. New Photocleavable Structures, 4. *Macromol. Rapid Commun.* **2008**, *29*, 57−62.
(57) Radebner, J.; Eibel, A.; Leypold, M.; Jungwirth, N.; Pickl, T.; Torvisco, A.; Fischer, R.; Fischer, U. K.; Moszner, N.; Gescheidt, G.; Stueger, H.; Haas, M. Tetraacylstannanes as Long-Wavelength Visible-Light Photoinitiators with Intriguing Low Toxicity. *Chem. - Eur. J.* **2018**, *24*, 8281−8285.
(58) Mitterbauer, M.; Knaack, P.; Naumov, S.; Markovic, M.; Ovsianikov, A.; Moszner, N.; Liska, R. Acylstannanes: Cleavable and

https://dx.doi.org/10.1021/acs.inorgchem.0c02181
Inorg. Chem. 2020, 59, 15204−15217

Highly Reactive Photoinitiators for Radical Photopolymerization at Wavelengths above 500 nm with Excellent Photobleaching Behavior. *Angew. Chem., Int. Ed.* **2018**, *57*, 12146−12150.
(59) Frühwirt, P.; Liška, A.; Wasdin, P. T.; Kelterer, A.-M.; Haas, M.; Ludvík, J.; Gescheidt, G. The "Dark Side" of Germanium-Based Photoinitiators—Connecting Redox Properties and Optical Absorption. *Organometallics* **2020**, *39*, 2257−2268.
(60) Gerson, F.; Huber, W. *Electron Spin Resonance Spectroscopy of Organic Radicals*; Wiley-VCH: Weinheim, 2003.
(61) Zalibera, M.; Stébé, P.-N.; Dietliker, K.; Grützmacher, H.; Spichty, M.; Gescheidt, G. The Redox Chemistry of Mono- and Bis(acyl)phosphane Oxides. *Eur. J. Org. Chem.* **2014**, *2014*, 331−337.
(62) Haas, M.; Leypold, M.; Schnalzer, D.; Torvisco, A.; Stueger, H. Stable Germenolates and Germenes with Exocyclic Structures. *Organometallics* **2015**, *34*, 5291−5297.
(63) Haas, M.; Leypold, M.; Schnalzer, D.; Torvisco, A.; Stueger, H. Synthesis and characterization of the first relatively stable dianionic germenolates. *Phosphorus, Sulfur Silicon Relat. Elem.* **2016**, *191*, 597−600.
(64) Haas, M. Recent Advances in the Chemistry of Heavier Group 14 Enolates. *Chem. - Eur. J.* **2019**, *25*, 15218−15227.
(65) Reichardt, C. *Solvents and Solvent Effects in Organic Chemistry*, 4th ed.; VCH: Weinheim, Germany, 2011.
(66) Eibel, A.; Radebner, J.; Haas, M.; Fast, D. E.; Freißmuth, H.; Stadler, E.; Faschauner, P.; Torvisco, A.; Lamparth, I.; Moszner, N.; Stueger, H.; Gescheidt, G. From mono- to tetraacylgermanes: extending the scope of visible light photoinitiators. *Polym. Chem.* **2018**, *9*, 38−47.
(67) Scaiano, J. C. Nanosecond Laser Flash Photolysis: A Tool for Physical Organic Chemistry. In *Reactive Intermediate Chemistry*; Platz, M., Moss, R. A., Jones, M., Eds.; Wiley-Interscience: Hoboken, NJ, 2004; pp 847−871.
(68) Lalevée, J.; Allonas, X.; Fouassier, J. P. Acylgermanes: Excited state processes and reactivity. *Chem. Phys. Lett.* **2009**, *469*, 298−303.
(69) Sluggett, G. W.; Turro, C.; George, M. W.; Koptyug, I. V.; Turro, N. J. (2,4,6-Trimethylbenzoyl)diphenylphosphine Oxide Photochemistry. A Direct Time-Resolved Spectroscopic Study of Both Radical Fragments. *J. Am. Chem. Soc.* **1995**, *117*, 5148−5153.
(70) Colley, C. S.; Grills, D. C.; Besley, N. A.; Jockusch, S.; Matousek, P.; Parker, A. W.; Towrie, M.; Turro, N. J.; Gill, P. M. W.; George, M. W. Probing the reactivity of photoinitiators for free radical polymerization: time-resolved infrared spectroscopic study of benzoyl radicals. *J. Am. Chem. Soc.* **2002**, *124*, 14952−14958.
(71) Jockusch, S.; Turro, N. J. Phosphinoyl Radicals: Structure and Reactivity. A Laser Flash Photolysis and Time-Resolved ESR Investigation. *J. Am. Chem. Soc.* **1998**, *120*, 11773−11777.
(72) Eibel, A.; Schmallegger, M.; Zalibera, M.; Huber, A.; Bürkl, Y.; Grützmacher, H.; Gescheidt, G. Extending the Scope of Bis(acyl)-phosphane Oxides: Additional Derivatives. *Eur. J. Inorg. Chem.* **2017**, *2017*, 2469−2478.
(73) *Scientific Documentation Bluephase Family − LED for Every Use*; Ivoclar Vivadent: Schaan, Liechtenstein.
(74) Stadler, E.; Eibel, A.; Fast, D.; Freißmuth, H.; Holly, C.; Wiech, M.; Moszner, N.; Gescheidt, G. A versatile method for the determination of photochemical quantum yields via online UV-Vis spectroscopy. *Photoch. Photobio. Sci.* **2018**, *17*, 660−669.
(75) Pangborn, A. B.; Giardello, M. A.; Grubbs, R. H.; Rosen, R. K.; Timmers, F. J. Safe and Convenient Procedure for Solvent Purification. *Organometallics* **1996**, *15*, 1518−1520.
(76) Brook, A. G.; Abdesaken, F.; Söllradl, H. Synthesis of some tris(trimethylsilyl)germyl compounds. *J. Organomet. Chem.* **1986**, *299*, 9−13.
(77) *Bruker APEX2 and SAINT*; Bruker AXS Inc.: Madison, WI, 2012.
(78) Blessing, R. H. An empirical correction for absorption anisotropy. *Acta Crystallogr., Sect. A: Found. Crystallogr.* **1995**, *51* (1), 33−38.
(79) Sheldrick, G. M. SADABS, version 2.10, *Siemens Area Detector Correction*; Universität Göttingen, Germany, 2003.
(80) Sheldrick, G. M. SHELXT - integrated space-group and crystal-structure determination. *Acta Crystallogr., Sect. A: Found. Adv.* **2015**, *71*, 3−8.
(81) Sheldrick, G. M. Phase annealing in SHELX-90: direct methods for larger structures. *Acta Crystallogr., Sect. A: Found. Crystallogr.* **1990**, *46*, 467−473.
(82) Sheldrick, G. M. A short history of SHELX. *Acta Crystallogr., Sect. A: Found. Crystallogr.* **2008**, *64*, 112−122.
(83) Sheldrick, G. M. Crystal structure refinement with SHELXL. *Acta Crystallogr., Sect. C: Struct. Chem.* **2015**, *71*, 3−8.
(84) Sheldrick, G. M. *SHELXS97*; Univ. Göttingen: Göttingen, Germany, 1997.
(85) Hübschle, C. B.; Sheldrick, G. M.; Dittrich, B. ShelXle: a Qt graphical user interface for SHELXL. *J. Appl. Crystallogr.* **2011**, *44*, 1281−1284.
(86) Spek, A. L. Single-crystal structure validation with the program PLATON. *J. Appl. Crystallogr.* **2003**, *36*, 7−13.
(87) Spek, A. L. Structure validation in chemical crystallography. *Acta Crystallogr., Sect. D: Biol. Crystallogr.* **2009**, *65*, 148−155.
(88) Spek, A. L. PLATON SQUEEZE: a tool for the calculation of the disordered solvent contribution to the calculated structure factors. *Acta Crystallogr., Sect. C: Struct. Chem.* **2015**, *71*, 9−18.
(89) van der Sluis, P.; Spek, A. L. BYPASS: an effective method for the refinement of crystal structures containing disordered solvent regions. *Acta Crystallogr., Sect. A: Found. Crystallogr.* **1990**, *46*, 194−201.
(90) Müller, P.; Herbst-Irmer, R.; Spek, A. L.; Schneider, T. R.; Sawaya, M. R. *Crystal Structure Refinement: A Crystallographer's Guide to SHELXL*; Oxford University Press, 2006; p 232.
(91) Neese, F. The ORCA program system. *Wiley Interdiscip. Rev.: Comput. Mol. Sci.* **2012**, *2*, 73−78.
(92) Becke, A. D. Density-functional thermochemistry. III. The role of exact exchange. *J. Chem. Phys.* **1993**, *98*, 5648−5652.
(93) Stephens, P. J.; Devlin, F. J.; Chabalowski, C. F.; Frisch, M. J. Ab Initio Calculation of Vibrational Absorption and Circular Dichroism Spectra Using Density Functional Force Fields. *J. Phys. Chem.* **1994**, *98*, 11623−11627.
(94) Grimme, S.; Antony, J.; Ehrlich, S.; Krieg, H. A consistent and accurate ab initio parametrization of density functional dispersion correction (DFT-D) for the 94 elements H-Pu. *J. Chem. Phys.* **2010**, *132*, 154104.
(95) Grimme, S.; Ehrlich, S.; Goerigk, L. Effect of the damping function in dispersion corrected density functional theory. *J. Comput. Chem.* **2011**, *32*, 1456−1465.
(96) Schäfer, A.; Horn, H.; Ahlrichs, R. Fully optimized contracted Gaussian basis sets for atoms Li to Kr. *J. Chem. Phys.* **1992**, *97*, 2571−2577.
(97) Weigend, F.; Häser, M.; Patzelt, H.; Ahlrichs, R. RI-MP2: optimized auxiliary basis sets and demonstration of efficiency. *Chem. Phys. Lett.* **1998**, *294*, 143−152.
(98) Barone, V.; Cossi, M. Quantum Calculation of Molecular Energies and Energy Gradients in Solution by a Conductor Solvent Model. *J. Phys. Chem. A* **1998**, *102*, 1995−2001.
(99) Allouche, A.-R. Gabedit–a graphical user interface for computational chemistry softwares. *J. Comput. Chem.* **2011**, *32*, 174−182.

https://dx.doi.org/10.1021/acs.inorgchem.0c02181
Inorg. Chem. 2020, 59, 15204−15217